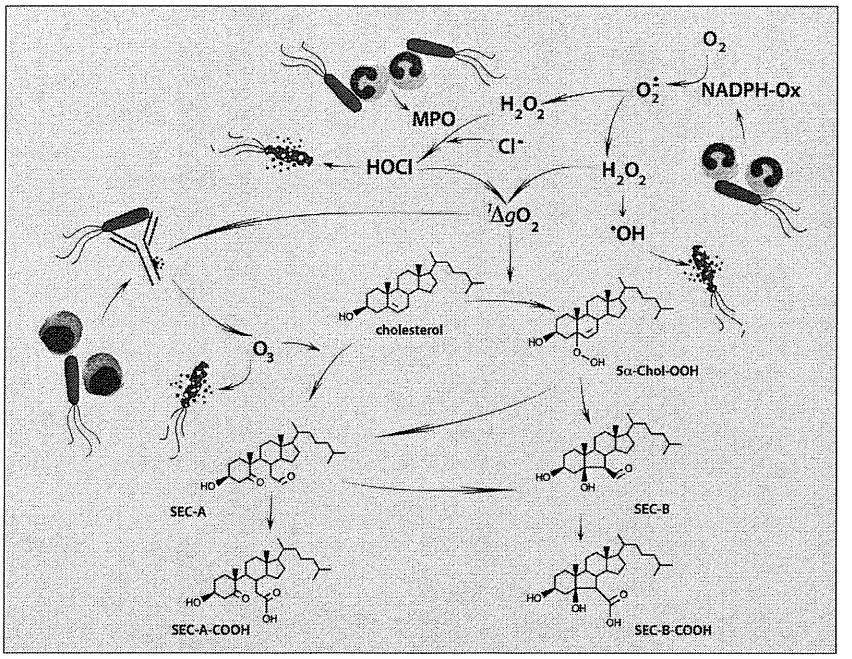

Fig. 1. Schematic representation of secosterols formation during the inflammatory response. Phagocytic cells recruited after a bacterial insult, are activated to produce highly reactive oxygen species through two enzymatic systems, i.e. NADPH-oxidase (NADPH-ox) and Myeloperoxidase (MPO) that contribute to bacterial killing. The formation of ozone by an antibody catalyzed reaction that uses singlet oxygen as substrate, has been proposed by Wentworth et al. [32,70,71] as an ancestral primary immune-response mechanism additional to the well-known superoxide-hydrogen peroxide-HOCl system. Ozone (O_3) and singlet oxygen ($^1\Delta gO_2$) may catalyze the formation of secosterols by promoting cholesterol autoxidation.

isolation of cholesteryl-9-oxononanoate and the subsequent appearance of both the fatty acid and cholesteryl moiety oxidation products, i.e. 9-oxononanoyl-sec-A and 9-oxononanoyl-sec-B [28]. These compounds derived from cholesterol/cholesterol esters ozonolysis exert potent biological activities including the denaturation of proteins and strong cytotoxicity in different cells lines (see below). High levels of sec-A and sec-B have been detected in human atherosclerotic plaques [29] and tissues samples of brains affected by neurodegeneration, such as Alzheimer's disease and Lewy body dementia [30,31], suggesting that increased formation of these compounds may be associated with inflammation-related diseases. Wentworth et al. [29] conducted pioneering works on secosterols and advised sec-A and sec-B as potential diagnostic markers of endogenous ozone production. They proposed a novel mechanisms for the unprecedented formation of ozone *in vivo* consisting of reactive oxygen species cascade (Fig. 1): (a) superoxide generation by activated neutrophil, (b) dismutation into hydrogen peroxide, (c) hypochlorous acid (HOCl) formation by myeloperoxidase (MPO), (d) singlet oxygen generation by the reaction of HOCl and hydrogen peroxide, and afterwards (e) formation of ozone from the singlet oxygen in an antibody-catalyzed water oxidation pathway [32,33]. A similar mechanism for the production of ozone-like reactive species from singlet oxygen in an amino acids-catalyzed water oxidation pathway was also reported [34]. However others have argued against the ozone-dependent mechanism of sec-A formation *in vivo* [35–37], and pointed out an alternative pathway for the formation of sec-A and sec-B. Uemi et al. [38] proposed a mechanism based on the Hock cleavage of 5α-Chol-OOH or a Chol-1,2-dioxetane intermediate formed by the reaction of cholesterol with singlet oxygen. Others provided evidence for sec-A and sec-B generation by the reaction of cholesterol with singlet oxygen produced by 1-methylnaphthalene-4-endoperoxide in phosphate buffer [39], and by the MPO–H_2O_2–Cl system [39]. Taken together these data point to a duplicate mechanism of sec-A and sec-B formation involving either ozone or singlet oxygen. Garner et al. [40] recently reported the development of a specific fluorogenic probes for ozone detections that, eventually, may help to investigate the role of ozone in pathophysiology. Being sec-B the predominant species formed during singlet oxygen-mediated cholesterol oxidation (sec-B is about 5–10 times higher than sec-A), the ratio sec-A to sec-B has been proposed as a surrogate measure to decipher the ozone-dependent and independent oxidation of cholesterol [39]. On the other hand, sec-A occurs as the dominant species formed by ozone in aqueous buffer system [41], and by phorbol-12-myristate-3-acetate-activated neutrophil in culture [27]. In addition, we were able to observe a time-dependent elevation of sec-A and sec-B in plasma after injecting lipopolysaccaride to C57BL/6j mice, but not in MPO-deficient mice. Besides, basal levels of sec-A and sec-B in the plasma of MPO-deficient mice were lower than the value found in wild type mice, but sec-A was barely detectable [27]. Sec-B was shown to be formed by aldolization of sec-A and, also, in an ozone-independent pathway via 5α-OOH-Chol or cholesterol-1,2-dioxetane [38]. Sec-B detected in the plasma of MPO-deficient mice, therefore, could be formed by the reaction of cholesterol with singlet oxygen generated *in vivo*, although its exact origin is currently unknown. Taken together these findings advise the occurrence of ozone-mediated reaction *in vivo* even if no conclusive evidences so far could be drawn for ozone production *in vivo*.

4. Biological activity of secosterols

The aldehydic function of secosterols is highly reactive and efficiently forms Schiff bases with ε- or N-terminal amino groups of proteins and with phosphatidylethanolamine, relevantly connected with atherosclerosis and a number of diseases associated with protein misfolding.

Wentworth et al. [29] reported that incubation of human LDL with either sec-A or sec-B led to time-dependent changes in the circular dichroism spectra of apoB-100, consistent with an altered

secondary structure, and increased atherogenicity, e.g. the secosterol-modified LDL was avidly taken up by macrophage leading to foam cell formation. Sec-A was shown to randomly modify the 6 different Lys residues of ApoC-II, as well as apolipoprotein that in the absence of lipids has conformational instability and undergoes fibrillization [42]. Sec-A accelerated ApoC-II polymerization with concurrent increase in thioflavin fluorescence [42], a signature of amyloidogenesis [43]. Interestingly, secA-COOH, which lacks the aldehydic functionality and is unable to form Schiff bases, was also able to accelerate ApoC-II fibril formation, albeit at a lesser extent, suggesting that non-covalent mechanisms may support secosterol-dependent ApoC-II amyloidogenesis [42]. These findings are relevant to the mechanisms of atherosclerosis because amyloid deposits are present in 50–60% of atherosclerotic lesions [44] and ApoC-II is a prominent component of these deposits [45]. Concentrations of secosterols are reportedly elevated in the cortex of patients with Lewy body dementia [31], a disease associated with intra-neuronal accumulation of α-synuclein in the form of amyloid fibrils or Lewy bodies. Sec-A, sec-B, and secoA-COOH have been shown to accelerate α-synuclein aggregation *in vitro*, and more interestingly secA-COOH was even more potent in forwarding the process [31]. Amyloidogenicity of amyloid-β (Aβ) is considered a crucial player of Alzheimer disease but an open question is the 2–3 order of magnitude disparity between the critical concentration to induce aggregation, which is in the micromolar range, and the actual concentration of Aβ at tissue level, which is in the nanomolar range [46]. Secosterols have been shown to effectively reduce below 100 nM the critical concentration of Aβ to aggregate [30,47]. Among the Aβ adducts with secosterol, Lys-16 Aβ modification formed amorphous aggregates fast and at very low concentrations of Aβ (20 nM), followed by the Lys-28 and Asp-1. Besides, the aggregates resulting from Lys-secosterols adducts were more toxic to primary rat cortical neuron [48]. Sec-A and sec-B in brain samples of patients affected by neurodegenerative disease approach concentrations of up 1 μM [30,49] that are suitable to covalently modify Aβ and increase its amyloidogenicity [30,31,47,50,51]. Sec-A and sec-B have been reported to induce structural change to myelin basic protein (MBP) relevant to the context of demyelinating diseases [52]. MBP accounts for approximately 30% of the total myelin protein, and is responsible for adhesion and stabilization of the intracellular surfaces of myelin layers. By reacting with MBP, secosterols have been shown to increase the surface exposure of the immunodominant epitope, decrease the surface exposure of the cathepsin D binding, and reduce the size and structural stability of MBP-induced aggregates. As a consequence of these alterations in the structure and function, MBP is unable to maintain the integrity of the myelin sheath and becomes vulnerable to autoimmune attack. In line to that which is observed with secosterol-initiated misfolding of Aβ and α-synuclein, sec-A and sec-B have been reported to induce misfolding of wild-type p53 [53]. The tumor suppressor protein p53 functions to maintain the integrity of the genome, and its activation in response to DNA damage promotes cell-cycle arrest in G1 phase or apoptosis. Upon incubation with secosterols, p53 undergoes polymerization that anticipates the formation of amyloid fibrillary aggregates. This misfolding renders p53 unable to bind to DNA and to induce transactivation of p21 [53]. Given that inflammation is the fuel for secosterols formation and that inflammation functions in all stages of tumor development, secosterols provide a chemical link to understand cancer carrying inactive p53.

Light-chain deposition disease is a severe, often fatal, clinical condition in which amyloid or amorphous deposits, as a consequence of antibody light chain aggregation, accumulate in the heart and/or kidney. Sec-A and sec-B have been reported to accelerate aggregation of human antibody kappa and lambda light chains *in vitro* under physiologically relevant conditions, causing an amorphous-type aggregation that is thioflavin and Congo red negative for both the kappa and lambda light chains [54]. Given the inflammatory microenvironment of secosterol production and its association with antibodies, the secosterol-induced protein misfolding is consistent with a pathophysiological role in light-chain deposition disease.

While the above reported studies show secosterols as playing deleterious roles by promoting misfolding of varied proteins, sec-B has unexpectedly been shown to inhibit the misfolding of a truncated murine mutant prion protein. Incubation of sec-B with a murine prion protein, paradoxically, induced stabilization of the native form of the prion and inhibited the generation of the disease-causing scrapie form [55]. The inhibition was specific for sec-B, where structural analogues were ineffective, offering a promising tool to develop new pharmacological active compounds to treat prion disease.

Additionally, secosterols have been reported to affect membrane and enzyme function. It was shown that secosterols bound phosphatidylethanolamine and phosphatidylserine via Schiff base formation, and also reduced biophysical parameters of membrane stability, which could be associated with various pathogenic insults [56–58]. Recently Genaro-Mattos and co-workers [59] reported that sec-B covalently bound and anchored cytochrome c to mitochondrial mimetic membranes, although its physiological role is still under investigation. Sec-A, but not sec-B, reportedly inhibited endothelial- and neuronal-type of nitric oxide synthase (NOS) activities, probably mediated by adduct formations with lysine residues on these enzymes [60]. The biochemical and biophysical properties of secosterols could be associated with their noxious activity on cells. Several studies have found that sec-A and sec-B induce cell death in various cell lines, including human B-lymphocytes (WI-L2), T-lymphocytes (Jurkat), vascular smooth muscle cells (VSMC), abdominal aorta endothelial cells (HAEC), murine tissue macrophages (J774.1), and an alveolar macrophage cell line (MH-S) [29]. Sathishkumar et al. [61] reported that sec-A exerted about 2-fold higher cytotoxicity than 5,6β-epoxy-Chol in hypothalamic neuron GT1-7 cells. Several pathways have been postulated for secosterol-triggered cell death, including the caspase-3/7-dependent pathway and the mitochondrial and death receptor pathway in cardiomyocyte H9c2 cells [62,63], the reactive oxygen species-dependent pathway in hypothalamic neuron GT1-7 cells [61,64], a mitochondrial death pathway in macrophage J774 cells, and the mitogen-activated protein kinase pathway in hepatocarcinoma HepG2 and Huh7 cells [65]. Moreover, secA-COOH and secB-COOH showed strong cytotoxic activities in human acute promyelocytic leukemia HL-60 cells [66]. Recently, it has been reported that 9-oxononanoyl-secA and 9-oxononanoyl-secB – ozonolysis products of cholesteryl-oleate and cholesteryl-linoleate present in human LDL – exert potent cytotoxicity towards HL-60 cells [28]. Their activity is stronger than other cytotoxic oxysterols, exhibiting EC50s of 10–20 μM, which were very similar against various cell lines tested.

5. *In vivo* detection

An overview of methods, biological samples investigated and levels of secosterols reported to date in the literature is shown in Table 1. For the analysis of sec-A and sec-B in biological or clinical samples, HPLC separation with UV, fluorescence, or MS detection have been widely employed. In general, lipid extracts of blood or tissue samples containing sec-A and sec-B are derivatized with hydrazine derivatives, such as dinitrophenylhydrazine (DNPH) [29,67,72]. To perform higher sensitivity detection, derivatization with dansyl hydrazine (DH, LOD = 1 fmol in [27,31,39]), 1-pyrenebutyric hydrazine (PBH; LOD = 10 fmol in [68]), Girard P (GP) hydra-

Table 1
Detections of sec-A and sec-B in biological samples.

Tissues/fluids	Species	Forms	Equipments	Concentrations	N	Ref
Lung	Rat (SD) exposed to ozone	Sec-A-DNPH	HPLC-UV	ND		72
		Sec-B-DNPH		ND		
Atherosclerotic plaque	Human	Sec-A-DNPH	HPLC-UV and LC-MS	6.8 - 61.3 pmol/mg	n=11	29
Plasma	Human (atherosclerotic patients)	Sec-B-DNPH		70 - 1690 nM	n=8	
Brain	Human (Alzheimer patients)	Sec-A-DNPH + Sec-B-DNPH	HPLC-UV and LC-MS	0.44 pmol/mg	n=4	30
	Human (Control)	Sec-A-DNPH + Sec-B-DNPH		0.35 pmol/mg	n=7	
Brain	Human (Lewy body dementia)	Sec-A-DNSL + Sec-B-DNSL	HPLC-F	0.21 uM	n=15	31
	Age-matched control	Sec-A-DNSL + Sec-B-DNSL		0.09 uM	n=18	
Brain	Rat	Sec-A-GP	LC-MS	~100 pg/mg		49
		Sec-B-GP		~300 pg/mg		
	Human	Sec-A-GP + Sec-B-GP		150 pg/mg		
Plasma	Mouse (C57BL/6)	Sec-A-DNSL	LC-MS/MS with IS (^{13}C-sec-A + ^{13}C-sec-B)	0.5 ± 0.2 nM	n=8	27
		Sec-B-DNSL		1.1 ± 0.3 nM	n=8	
	Mouse (C57BL/6 MPO-KO)	Sec-A-DNSL		0.03 ± 0.1 nM	n=7	
		Sec-B-DNSL		0.5 ± 0.4 nM	n=7	
Liver	Mouse (C57BL/6)	Sec-B-DNSL		126.0 ± 42.7 pmol/g	n=8	
	Mouse (C57BL/6 MPO-KO)	Sec-B-DNSL		62.2 ± 21.6 pmol/g	n=7	
Plasma	Human (healthy volunteers)	Sec-A-HMP	LC-MS/MS with IS (^{13}C-sec-A + ^{13}C-sec-B)	23.6 ± 16.6 nM	n=10	69
		Sec-B-HMP		27.3 ± 41.0 nM	n=10	
	Mouse (C57BL/6)	Sec-A-HMP		1.4 ± 0.7 pmol/g	n=3	
		Sec-B-HMP		4.3 ± 0.8 pmol/g	n=3	
Brain		Sec-A-HMP		10.4 ± 16.3 pmol/g	n=3	
		Sec-B-HMP		110.9 ± 10.6 pmol/g	n=3	
Liver		Sec-A-HMP		34.1 ± 21.6 pmol/g	n=3	
		Sec-B-HMP		161.5 ± 56.3 pmol/g	n=3	
Lung		Sec-A-HMP		29.1 ± 1.3 pmol/g	n=3	
		Sec-B-HMP		80.4 ± 1.4 pmol/g	n=3	

zine (LOD = 2.7 fmol in [49]), or 2-hydrazino-1-methylpyridine (HMP; LOD = 10–50 amol in [69]). Using these derivatizing reagents, sec-A and sec-B present in blood or tissues were detectable as secosterol–hydrazone derivatives by HPLC-fluorescence detector and LC–MS (Table 1). Griffiths and co-workers reported levels of sec-A and sec-B in rat brain of ~100 pg/mg (240 pmol/g) and ~300 pg/mg (720 pmol/g), respectively, determined after derivatization with GP hydrazine [49]. Sec-A and sec-B in human brain were also analyzed by HPLC-UV or LC–MS after derivatization with DNPH resulting in levels of (sec-A + sec-B) 0.44 pmol/mg in Alzheimer's patients ($n = 4$) and 0.35 pmol/mg in control subjects ($n = 7$) [30]. In addition, increased levels of secosterols (sec-A + sec-B) were observed in the cortex of brain affected by Lewy body dementia (0.213 μM, $n = 15$) compared to those of age-matched controls (0.093 μM, $n = 18$) in analysis done by HPLC-fluorescence detector and LC–MS after DH derivatization [31]. Wentworth and co-worker analyzed DNPH-derivatives of sec-A and sec-B in organic extracts of human atherosclerotic plaque by LC–MS, and found them in the ranges of 6.8–61.3 pmol/mg plaque [29]. Elevated levels of sec-B were also observed in the plasma of these patients (70–1690 nM) compared to those of controls subjects [29]. We have recently developed a highly sensitive isotope dilution method to detect sec-A and sec-B as HMP derivatives by LC–ESI–MS/MS, and using 3,4-^{13}C-sec-A and 3,4-^{13}C-sec-B as internal standards [69]. We found levels of sec-A and sec-B of 23.6 ± 16.6 nM and 27.3 ± 41.0 nM, respectively, in human plasma ($n = 10$). The levels of sec-A and sec-B were respectively 1.4 ± 0.7 and 4.3 ± 0.8 nM in the plasma, 10.4 ± 16.3 and 110.9 ± 10.6 pmol/g in the brain, 34.1 ± 21.6 and 161.5 ± 56.3 pmol/g in the liver and 29.1 ± 1.3, and 80.4 ± 1.4 pmol/g in the lung of C57BL/6j mice ($n = 3$). In addition, ozonolysis products of cholesteryl-oleate and cholesteryl-linoleate, 9-oxononanoyl-sec-A and 9-oxononanoyl-sec-B, were found in human LDL at levels of 16.5 ± 5.4 and 11.3 ± 3.9 pmol/mg LDL protein, respectively [28]. Notably, the values of cholesterol aldehydes in biological samples differ widely among the different laboratories. As sec-A is very unstable, at least the use of stable-isotope labeled internal standards in secosterol analysis is mandatory.

Although formation mechanisms of secosterols are not still fully unveiled, elevated levels of secosterols have been observed in various tissues collected from different inflammatory diseases. Sec-A, sec-B, and other related compounds including secA-COOH, secB-COOH, and 9-oxononanoyl secosterols exert strong biological activities compared to other oxysterols. Further studies are warranted to elucidate the mechanisms of secosterols formation *in vivo* and their pathological roles in relation to pathogenesis of several inflammatory diseases.

Acknowledgments

This work was supported in part by JSPS KAKENHI Grants (24680075 to NM, 24700838 to ST, and 24300257 to HO).

References

[1] I.A. Pikuleva, Cholesterol-metabolizing cytochromes P450: implications for cholesterol lowering, Expert Opin. Drug Metab. Toxicol. 4 (2008) 1403–1414.
[2] I. Bjorkhem, G. Eggertsen, Genes involved in initial steps of bile acid synthesis, Curr. Opin. Lipidol. 12 (2001) 97–103.
[3] I. Bjorkhem, E. Reihner, B. Angelin, S. Ewerth, J.E. Akerlund, K. Einarsson, On the possible use of the serum level of 7alpha-hydroxycholesterol as a marker for increased activity of the cholesterol 7alpha-hydroxylase in humans, J. Lipid Res. 28 (1987) 889–894.
[4] A. Lovgren-Sandblom, M. Heverin, H. Larsson, E. Lundstrom, J. Wahren, U. Diczfalusy, I. Bjorkhem, Novel LC–MS/MS method for assay of 7alpha-hydroxy-4-cholesten-3-one in human plasma. Evidence for a significant extrahepatic metabolism, J. Chromatogr. B: Anal. Technol. Biomed. Life Sci. 856 (2007) 15–19.
[5] U. Diczfalusy, J. Miura, H.K. Roh, R.A. Mirghani, J. Sayi, H. Larsson, K.G. Bodin, A. Allqvist, M. Jande, J.W. Kim, E. Aklillu, L.L. Gustafsson, L. Bertilsson, 4Beta-hydroxycholesterol is a new endogenous CYP3A marker: relationship to CYP3A5 genotype, quinine 3-hydroxylation and sex in Koreans, Swedes and Tanzanians, Pharmacogenet. Genomics 18 (2008) 201–208.
[6] D. Lutjohann, O. Breuer, G. Ahlborg, I. Nennesmo, A. Siden, U. Diczfalusy, I. Bjorkhem, Cholesterol homeostasis in human brain: evidence for an age-dependent flux of 24S-hydroxycholesterol from the brain into the circulation, Proc. Natl. Acad. Sci. U S A 93 (1996) 9799–9804.

[7] Y. Ohyama, S. Meaney, M. Heverin, L. Ekstrom, A. Brafman, M. Shafir, U. Andersson, M. Olin, G. Eggertsen, U. Diczfalusy, E. Feinstein, I. Bjorkhem, Studies on the transcriptional regulation of cholesterol 24-hydroxylase (CYP46A1): marked insensitivity toward different regulatory axes, J. Biol. Chem. 281 (2006) 3810–3820.
[8] N.B. Javitt, 25R,26-Hydroxycholesterol revisited: synthesis, metabolism, and biologic roles, J. Lipid Res. 43 (2002) 665–670.
[9] N.B. Javitt, Oxysteroids: a new class of steroids with autocrine and paracrine functions, Trends Endocrinol. Metab. 15 (2004) 393–397.
[10] E.G. Lund, T.A. Kerr, J. Sakai, W.P. Li, D.W. Russell, cDNA cloning of mouse and human cholesterol 25-hydroxylases, polytopic membrane proteins that synthesize a potent oxysterol regulator of lipid metabolism, J. Biol. Chem. 273 (1998) 34316–34327.
[11] J. Wong, C.M. Quinn, A.J. Brown, Synthesis of the oxysterol, 24(S), 25-epoxycholesterol, parallels cholesterol production and may protect against cellular accumulation of newly-synthesized cholesterol, Lipids Health Dis. 6 (2007) 10.
[12] G. Segala, Medina P. de, L. Iuliano, C. Zerbinati, M.R. Paillasse, E. Noguer, F. Dalenc, B. Payre, V.C. Jordan, M. Record, S. Silvente-Poirot, M. Poirot, 5,6-Epoxy-cholesterols contribute to the anticancer pharmacology of tamoxifen in breast cancer cells, Biochem. Pharmacol. 86 (2013) 175–189.
[13] L. Iuliano, Pathways of cholesterol oxidation via non-enzymatic mechanisms, Chem. Phys. Lipids 164 (2011) 457–468.
[14] A.W. Girotti, Lipid hydroperoxide generation, turnover, and effector action in biological systems, J. Lipid Res. 39 (1998) 1529–1542.
[15] O. Wintersteiner, S. Bergström, The products formed by the action of oxygen on colloidal solutions of cholesterol, J. Biol. Chem. 137 (1941) 785–786.
[16] H.W. Gardner, Oxygen radical chemistry of polyunsaturated fatty acids, Free Radical Biol. Med. 7 (1989) 65–86.
[17] D. Neshchadin, F. Palumbo, M.S. Sinicropi, I. Andreu, G. Gescheidta, M.A. Miranda, Topological control in radical reactions of cholesterol in model dyads, Chem. Sci. 4 (2013) 1608–1614.
[18] L. Xu, Z. Korade, N.A. Porter, Oxysterols from free radical chain oxidation of 7-dehydrocholesterol: product and mechanistic studies, J. Am. Chem. Soc. 132 (2010) 2222–2232.
[19] W. Korytowski, M. Wrona, A.W. Girotti, Radiolabeled cholesterol as a reporter for assessing one-electron turnover of lipid hydroperoxides, Anal. Biochem. 270 (1999) 123–132.
[20] J. Gumulka, L.L. Smith, Ozonization of cholesterol, J. Am. Chem. Soc. 105 (1983) 1972–1979.
[21] L.J. Athelstan, J. Beckwith, A.G. Davies, I.G.E. Davison, A. Maccoll, M.H. Mruzek, The mechanism of the rearrangement of allylic hydroperoxides 5α-hydroperoxy-3-β-hydroxycholest-6ene- and 7α-hydroperoxy-3-beta-hydroxycholest-5-ene, J. Chem. Soc., Perkin Trans. 22 (1989) 815–824.
[22] W. Korytowski, G.J. Bachowski, A.W. Girotti, Photoperoxidation of cholesterol in homogeneous solution, isolated membranes, and cells: comparison of the 5 alpha- and 6 beta-hydroperoxides as indicators of singlet oxygen intermediacy, Photochem. Photobiol. 56 (1992) 1–8.
[23] W. Korytowski, P.G. Geiger, A.W. Girotti, Lipid hydroperoxide analysis by high-performance liquid chromatography with mercury cathode electrochemical detection, Methods Enzymol. 300 (1999) 23–33.
[24] J.P. Thomas, A.W. Girotti, Photooxidation of cell membranes in the presence of hematoporphyrin derivative: reactivity of phospholipid and cholesterol hydroperoxides with glutathione peroxidase, Biochim. Biophys. Acta 962 (1988) 297–307.
[25] J.P. Thomas, M. Maiorino, F. Ursini, A.W. Girotti, Protective action of phospholipid hydroperoxide glutathione peroxidase against membrane-damaging lipid peroxidation. In situ reduction of phospholipid and cholesterol hydroperoxides, J. Biol. Chem. 265 (1990) 454–461.
[26] J.P. Thomas, P.G. Geiger, M. Maiorino, F. Ursini, A.W. Girotti, Enzymatic reduction of phospholipid and cholesterol hydroperoxides in artificial bilayers and lipoproteins, Biochim. Biophys. Acta 1045 (1990) 252–260.
[27] S. Tomono, N. Miyoshi, H. Shiokawa, T. Iwabuchi, Y. Aratani, T. Higashi, H. Nukaya, H. Ohshima, Formation of cholesterol ozonolysis products in vitro and in vivo through a myeloperoxidase-dependent pathway, J. Lipid Res. 52 (2011) 87–97.
[28] N. Miyoshi, N. Iwasaki, S. Tomono, T. Higashi, H. Ohshima, Occurrence of cytotoxic 9-oxononanoyl secosterol aldehydes in human low-density lipoprotein, Free Radical Biol. Med. 60 (2013) 73–79.
[29] P. Wentworth Jr., J. Nieva, C. Takeuchi, R. Galve, A.D. Wentworth, R.B. Dilley, G.A. DeLaria, A. Saven, B.M. Babior, K.D. Janda, A. Eschenmoser, R.A. Lerner, Evidence for ozone formation in human atherosclerotic arteries, Science 302 (2003) 1053–1056.
[30] Q. Zhang, E.T. Powers, J. Nieva, M.E. Huff, M.A. Dendle, J. Bieschke, C.G. Glabe, A. Eschenmoser, P. Wentworth Jr., R.A. Lerner, J.W. Kelly, Metabolite-initiated protein misfolding may trigger Alzheimer's disease, Proc. Natl. Acad. Sci. U S A 101 (2004) 4752–4757.
[31] D.A. Bosco, D.M. Fowler, Q. Zhang, J. Nieva, E.T. Powers, P. Wentworth Jr., R.A. Lerner, J.W. Kelly, Elevated levels of oxidized cholesterol metabolites in Lewy body disease brains accelerate alpha-synuclein fibrilization, Nat. Chem. Biol. 2 (2006) 249–253.
[32] P. Wentworth Jr., J.E. McDunn, A.D. Wentworth, C. Takeuchi, J. Nieva, T. Jones, C. Bautista, J.M. Ruedi, A. Gutierrez, K.D. Janda, B.M. Babior, A. Eschenmoser, R.A. Lerner, Evidence for antibody-catalyzed ozone formation in bacterial killing and inflammation, Science 298 (2002) 2195–2199.
[33] B.M. Babior, C. Takeuchi, J. Ruedi, A. Gutierrez, P. Wentworth Jr., Investigating antibody-catalyzed ozone generation by human neutrophils, Proc. Natl. Acad. Sci. U S A 100 (2003) 3031–3034.
[34] K. Yamashita, T. Miyoshi, T. Arai, N. Endo, H. Itoh, K. Makino, K. Mizugishi, T. Uchiyama, M. Sasada, Ozone production by amino acids contributes to killing of bacteria, Proc. Natl. Acad. Sci. U S A 105 (2008) 16912–16917.
[35] H. Sies, Ozone in arteriosclerotic plaques: searching for the "smoking gun", Angew. Chem., Int. Ed. Engl. 43 (2004) 3514–3515.
[36] L.L. Smith, Oxygen, oxysterols, ouabain, and ozone: a cautionary tale, Free Radical Biol. Med. 37 (2004) 318–324.
[37] W.A. Pryor, K.N. Houk, C.S. Foote, J.M. Fukuto, L.J. Ignarro, G.L. Squadrito, K.J. Davies, Free radical biology and medicine: it's a gas, man!, Am J. Physiol. Regul. Integr. Comp. Physiol. 291 (2006) R491–R511.
[38] M. Uemi, G.E. Ronsein, S. Miyamoto, M.H. Medeiros, Mascio P. Di, Generation of cholesterol carboxyaldehyde by the reaction of singlet molecular oxygen [O_2 ($^1\Delta_g$)] as well as ozone with cholesterol, Chem. Res. Toxicol. 22 (2009) 875–884.
[39] S. Tomono, N. Miyoshi, K. Sato, Y. Ohba, H. Ohshima, Formation of cholesterol ozonolysis products through an ozone-free mechanism mediated by the myeloperoxidase–H_2O_2–chloride system, Biochem. Biophys. Res. Commun. 383 (2009) 222–227.
[40] A.L. Garner, C.M. St Croix, B.R. Pitt, G.D. Leikauf, S. Ando, K. Koide, Specific fluorogenic probes for ozone in biological and atmospheric samples, Nat. Chem. 1 (2009) 316–321.
[41] A.D. Wentworth, B.D. Song, J. Nieva, A. Shafton, S. Tripurenani, P. Wentworth Jr., The ratio of cholesterol 5,6-secosterols formed from ozone and singlet oxygen offers insight into the oxidation of cholesterol in vivo, Chem. Commun. (Cambridge, U.K.) 21 (2009) 3098–3100.
[42] C.R. Stewart, L.M. Wilson, Q. Zhang, C.L. Pham, L.J. Waddington, M.K. Staples, D. Stapleton, J.W. Kelly, G.J. Howlett, Oxidized cholesterol metabolites found in human atherosclerotic lesions promote apolipoprotein C-II amyloid fibril formation, Biochemistry 46 (2007) 5552–5561.
[43] D.M. Hatters, C.E. MacPhee, L.J. Lawrence, W.H. Sawyer, G.J. Howlett, Human apolipoprotein C-II forms twisted amyloid ribbons and closed loops, Biochemistry 39 (2000) 8276–8283.
[44] C. Rocken, J. Tautenhahn, F. Buhling, D. Sachwitz, S. Vockler, A. Goette, T. Burger, Prevalence and pathology of amyloid in atherosclerotic arteries, Arterioscler. Thromb. Vasc. Biol. 26 (2006) 676–677.
[45] L.A. Medeiros, T. Khan, J.B. El Khoury, C.L. Pham, D.M. Hatters, G.J. Howlett, R. Lopez, K.D. O'Brien, K.J. Moore, Fibrillar amyloid protein present in atheroma activates CD36 signal transduction, J. Biol. Chem. 279 (2004) 10643–10648.
[46] P.D. Mehta, T. Pirttila, B.A. Patrick, M. Barshatzky, S.P. Mehta, Amyloid beta protein 1–40 and 1–42 levels in matched cerebrospinal fluid and plasma from patients with Alzheimer disease, Neurosci. Lett. 304 (2001) 102–106.
[47] J. Bieschke, Q. Zhang, E.T. Powers, R.A. Lerner, J.W. Kelly, Oxidative metabolites accelerate Alzheimer's amyloidogenesis by a two-step mechanism, eliminating the requirement for nucleation, Biochemistry 44 (2005) 4977–4983.
[48] K. Usui, J.D. Hulleman, J.F. Paulsson, S.J. Siegel, E.T. Powers, J.W. Kelly, Site-specific modification of Alzheimer's peptides by cholesterol oxidation products enhances aggregation energetics and neurotoxicity, Proc. Natl. Acad. Sci. U S A 106 (2009) 18563–18568.
[49] K. Karu, M. Hornshaw, G. Woffendin, K. Bodin, M. Hamberg, G. Alvelius, J. Sjovall, J. Turton, Y. Wang, W.J. Griffiths, Liquid chromatography-mass spectrometry utilizing multi-stage fragmentation for the identification of oxysterols, J. Lipid Res. 48 (2007) 976–987.
[50] H. Komatsu, L. Liu, I.V. Murray, P.H. Axelsen, A mechanistic link between oxidative stress and membrane mediated amyloidogenesis revealed by infrared spectroscopy, Biochim. Biophys. Acta 1768 (2007) 1913–1922.
[51] I.V. Murray, L. Liu, H. Komatsu, K. Uryu, G. Xiao, J.A. Lawson, P.H. Axelsen, Membrane-mediated amyloidogenesis and the promotion of oxidative lipid damage by amyloid beta proteins, J. Biol. Chem. 282 (2007) 9335–9345.
[52] N.K. Cygan, J.C. Scheinost, T.D. Butters, P. Wentworth Jr., Adduction of cholesterol 5,6-secosterol aldehyde to membrane-bound myelin basic protein exposes an immunodominant epitope, Biochemistry 50 (2011) 2092–2100.
[53] J. Nieva, B.D. Song, J.K. Rogel, D. Kujawara, L. Altobel 3rd, A. Izharrudin, G.E. Boldt, R.K. Grover, A.D. Wentworth, P. Wentworth Jr., Cholesterol secosterol aldehydes induce amyloidogenesis and dysfunction of wild-type tumor protein p53, Chem. Biol. 18 (2011) 920–927.
[54] J. Nieva, A. Shafton, L.J. Altobell 3rd, S. Tripuraneni, J.K. Rogel, A.D. Wentworth, R.A. Lerner, P. Wentworth Jr., Lipid-derived aldehydes accelerate light chain amyloid and amorphous aggregation, Biochemistry 47 (2008) 7695–7705.
[55] J.C. Scheinost, D.P. Witter, G.E. Boldt, J. Offer, P. Wentworth Jr., Cholesterol secosterol adduction inhibits the misfolding of a mutant prion protein fragment that induces neurodegeneration, Angew. Chem., Int. Ed. Engl. 48 (2009) 9469–9472.
[56] E. Wachtel, D. Bach, R.F. Epand, A. Tishbee, R.M. Epand, A product of ozonolysis of cholesterol alters the biophysical properties of phosphatidylethanolamine membranes, Biochemistry 45 (2006) 1345–1351.
[57] D. Bach, E. Wachtel, I.R. Miller, Kinetics of Schiff base formation between the cholesterol ozonolysis product 3-beta-hydroxy-5-oxo-5,6-secocholestan-6-al and phosphatidylethanolamine, Chem. Phys. Lipids 157 (2009) 51–55.
[58] D. Bach, R.F. Epand, R.M. Epand, I.R. Miller, E. Wachtel, The oxysterol 3beta-hydroxy-5-oxo-5,6-secocholestan-6-al changes the phase behavior and

structure of phosphatidylethanolamine–phosphatidylcholine mixtures, Chem. Phys. Lipids 164 (2011) 672–679.

[59] T.C. Genaro-Mattos, P.P. Appolinario, K.C. Mugnol, C. Bloch Jr., I.L. Nantes, Mascio.P. Di, S. Miyamoto, Covalent binding and anchoring of cytochrome c to mitochondrial mimetic membranes promoted by cholesterol carboxyaldehyde, Chem. Res. Toxicol. 26 (2013) 1536–1544.

[60] Y.L. Lai, S. Tomono, N. Miyoshi, H. Ohshima, Inhibition of endothelial- and neuronal-type, but not inducible-type, nitric oxide synthase by the oxidized cholesterol metabolite secosterol aldehyde: implications for vascular and neurodegenerative diseases, J. Clin. Biochem. Nutr. 50 (2012) 84–89.

[61] K. Sathishkumar, S.N. Murthy, R.M. Uppu, Cytotoxic effects of oxysterols produced during ozonolysis of cholesterol in murine GT1-7 hypothalamic neurons, Free Radical Res. 41 (2007) 82–88.

[62] K. Sathishkumar, M. Haque, T.E. Perumal, J. Francis, R.M. Uppu, A major ozonation product of cholesterol, 3β-hydroxy-5-oxo-5,6-secocholestan-6-al, induces apoptosis in H9c2 cardiomyoblasts, FEBS Lett. 579 (2005) 6444–6450.

[63] K. Sathishkumar, X. Gao, A.C. Raghavamenon, N. Parinandi, W.A. Pryor, R.M. Uppu, Cholesterol secoaldehyde induces apoptosis in H9c2 cardiomyoblasts through reactive oxygen species involving mitochondrial and death receptor pathways, Free Radical Biol. Med. 47 (2009) 548–558.

[64] K. Sathishkumar, X. Xi, R. Martin, R.M. Uppu, Cholesterol secoaldehyde, an ozonation product of cholesterol, induces amyloid aggregation and apoptosis in murine GT1-7 hypothalamic neurons, J. Alzheimers Dis. 11 (2007) 261–274.

[65] S. Anticoli, M. Arciello, A. Mancinetti, Martinis.M. De, L. Ginaldi, L. Iuliano, C. Balsano, 7-Ketocholesterol and 5,6-secosterol modulate differently the stress-activated mitogen-activated protein kinases (MAPKs) in liver cells, J. Cell Physiol. 222 (2010) 586–595.

[66] S. Tomono, Y. Yasue, N. Miyoshi, H. Ohshima, Cytotoxic effects of secosterols and their derivatives on several cultured cells, Biosci. Biotechnol. Biochem. 77 (2013) 651–653.

[67] K. Wang, E. Bermudez, W.A. Pryor, The ozonation of cholesterol: separation and identification of 2,4-dinitrophenylhydrazine derivatization products of 3 beta-hydroxy-5-oxo-5,6-secocholestan-6-al, Steroids 58 (1993) 225–229.

[68] F.V. Mansano, R.M. Kazaoka, G.E. Ronsein, F.M. Prado, T.C. Genaro-Mattos, M. Uemi, Mascio.P. Di, S. Miyamoto, Highly sensitive fluorescent method for the detection of cholesterol aldehydes formed by ozone and singlet molecular oxygen, Anal. Chem. 82 (2010) 6775–6781.

[69] S. Tomono, N. Miyoshi, M. Ito, T. Higashi, H. Ohshima, A highly sensitive LC–ESI–MS/MS method for the quantification of cholesterol ozonolysis products secosterol-A and secosterol-B after derivatization with 2-hydrazino-1-methylpyridine, J. Chromatogr., B: Anal. Technol. Biomed. Life Sci. 879 (2011) 2802–2808.

[70] D. Datta, N. Vaidehi, X. Xu, W.A. Goddard 3rd, Mechanism for antibody catalysis of the oxidation of water by singlet dioxygen, Proc. Natl. Acad. Sci. U S A 99 (2002) 2636–2641.

[71] A.D. Wentworth, L.H. Jones, P. Wentworth Jr., K.D. Janda, R.A. Lerner, Antibodies have the intrinsic capacity to destroy antigens, Proc. Natl. Acad. Sci. U S A 97 (2000) 10930–10935.

[72] W.A. Pryor, K. Wang, E. Bermudez, Cholesterol ozonation products as biomarkers for ozone exposure in rats, Biochem. Biophys. Res. Commun. 188 (1992) 618–623.

The Journal of Toxicological Sciences (J. Toxicol. Sci.)
Vol.39, No.3, 499-505, 2014

Original Article

MWCNT causes extensive damage to the ciliated epithelium of the trachea of rodents

Teruya Ohba[1], Jiegou Xu[2], David B. Alexander[2], Akane Yamada[1], Jun Kanno[3], Akihiko Hirose[4], Hiroyuki Tsuda[2] and Yuji Imaizumi[1]

[1]Department of Molecular and Cellular Pharmacology, Nagoya City University Graduate School of Pharmaceutical Sciences, 3-1 Tanabedori, Mizuhoku, Nagoya 467-8603, Japan
[2]Laboratory of Nanotoxicology, Nagoya City University, 3-1 Tanabedori, Mizuhoku, Nagoya 467-8603, Japan
[3]Division of Cellular and Molecular Toxicology, 1-18-1 Kamiyoga, Setagaya-ku, Tokyo 158-8501, Japan
[4]Division of Risk Assessment, National Institute of Health Sciences, 1-18-1 Kamiyoga, Setagaya-ku, Tokyo 158-8501, Japan

(Received February 19, 2014; Accepted April 8, 2014)

ABSTRACT — The ciliated tracheobronchial epithelium plays an important role in the excretion of inhaled dust. While many reports indicate that inhaled multi-walled carbon nanotubes (MWCNT) induce inflammation and proliferative changes in the lung and pleura, their effects on the upper airway have not been reported. Two different types of MWCNTs, MWCNT-L (8 μm in length and 150 nm in diameter) and MWCNT-S (3 μm in length and 15 nm in diameter), were examined for their effect on the trachea as well as the bronchus and lung. In vitro, the movement of the cilia of primary tracheal epithelial cells was impaired by treatment with the 2 MWCNTs. Rats were treated with 0.3 ml of a 250 μg/ml suspension of MWCNTs on days 1, 4, and 7, and sacrificed on day 8. Extensive loss of ciliated cells and replacement by flat cells without cilia was observed in the trachea. Deposition of MWCNTs and occasional squamous cell metaplasia were found in the regenerative granulation tissue. The proportion of the lesion to the transverse section of the trachea was vehicle, 0; MWCNT-L, 27.2 ± 10.5; MWCNT-S, 32.1 ± 15.8 (both MWCNTs, $p < 0.001$ vs vehicle). The amount of cilia showed significant decrease in the MWCNT-L treated rats ($p < 0.05$). In contrast to the trachea lesions, the number of inflammatory foci in the lung was greater in the MWCNT-S than in the MWCNT-L treated rats. Our results indicate that both MWCNTs caused extensive damage to the ciliated epithelium of the trachea. This damage may prolong the deposition of inhaled MWNCT in the lung.

Key words: MWCNT, Tracheal damage, Ciliated epithelium, Rat

INTRODUCTION

Multi-walled carbon nanotubes (MWCNT) are a newly developed material with potential applications in many fields including the biomedical field. The high aspect ratio of MWCNT is similar to that of asbestos and has led to concern that exposure to MWCNT might cause asbestos-like lung diseases (Bonner, 2010; Donaldson et al., 2010; Nagai and Toyokuni, 2010). Many reports have indicated that exposure of rats to MWCNT induces inflammation, fibrosis and oxidative stress in the lung and pleura (Mercer et al., 2010, 2013; Xu et al., 2012). To date, in vivo studies have focused on the toxicity of MWCNT in the lung and pleura, and nothing has been reported regarding the effect of MWCNT on the epithelium of the trachea.

The tracheal and primary branch of the bronchial epithelium is mainly composed of ciliated cells and some goblet cells. The ciliated cells are responsible for carrying out inhaled dust particles in the throat by their ciliary transportation movement. Thus, the ciliated cells play a pivotal role in the defense of the airway against inhaled particle matter. Several environmental factors such as cigarette smoke (Simet et al., 2010) and diesel gas particles (Li et al., 2011) have been shown to impair ciliated cell functions, resulting in increased pulmonary deposition. Zinc oxide nanoparticles have been reported to induce proliferation of airway epithelial cells and goblet cell hyperplasia (Cho et al., 2011) and transient epithelial hyperplasia of the terminal bronchiole (Xu et al.,

Correspondence: Yuji Imaizumi (E-mail: yimaizum@phar.nagoya-cu.ac.jp)

2014). Although several reports indicate that MWCNT have some toxic effects on bronchial epithelial cells in vitro (Hirano et al., 2010; Lindberg et al., 2009; Rotoli et al., 2008), the effect on the upper airway in animals remains unknown. In the present study, we investigated the effects of MWCNT on the tracheal epithelium in vitro and in vivo and the bronchus and lung in vivo after short-term exposure.

MATERIALS AND METHODS

Animals

8-12 week old C57BL/6N male mice (Japan SLC Inc., Shizuoka, Japan) and 6-7 week old Wistar/ST rats were obtained from Japan SLC Inc. Rats were housed in the Animal Center of Nagoya City University Graduate School of Pharmaceutical Sciences and maintained on a 12 hr light/12 hr dark cycle and received Oriental MF basal diet (Oriental Yeast Co. Ltd., Tokyo, Japan) and water ad libitum. The study was conducted according to the Guidelines for the Care and Use of Laboratory Animals of Nagoya City University Graduate School of Pharmaceutical Sciences, and the experimental protocol was approved by the Nagoya City University Animal Care and Use Committee (H24-p-12).

Preparation of MWCNT and Fluorescent Microspheres (FMS)

We used two types of MWCNTs, MWCNT-L and MWCNT-S, which are grown in the vapor phase. According to the manufacturer's information, the primary size of MWCNT-L is 150 nm in mean diameter and 8 μm in mean length, and the primary size of MWCNT-S is 15 nm in mean diameter and 3 μm in mean length. Five milligrams of MWCNT-L or MWCNT-S were suspended in 20 ml of saline containing 0.5% Pluronic F68 (PF68, non-ionic, biocompatible amphiphillic block copolymers, Sigma-Aldrich, St Louis, MO, USA) and homogenized for 1 min at 3,000 rpm in a Polytron PT1600E benchtop homogenizer (Kinematika AG, Littau, Switzerland) 4 times. The suspensions were sonicated for 30 min shortly before use to minimize aggregation. The concentration of the MWCNTs was 250 μg/ml. Both MWCNT-L and MWCNT-S dispersed well in the vehicle solution. MWCNT-L showed single fibers with a needle-like shape under scanning electron microscope (SEM) observation, but gradually formed agglomerates over time. Since MWCNT-S are tangled fibers, it showed cotton-like aggregation in suspension under SEM observation. However, they did not form larger agglomerates: incubation in suspension up to 7 days (data not shown). Fluorescent Microspheres (FMS) were purchased from Invitrogen (TetraSpeckTM microspheres, 500 nm in diameter) and suspended by sonication at 250 μg/ml in saline containing 0.5% PF68.

Isolation of single ciliated cells

Isolation of single ciliated cells was as previously reported (Ma et al., 2006). Briefly, the tracheal epithelium was separated from the cartilage and cut into pieces of approximately 0.1 × 0.1 cm. The tissue was incubated in phosphate-buffered saline containing NaCl 137 mM, KCl 2.7 mM, $CaCl_2$ 0.9 mM, $MgCl_2$ 0.5 mM, Na_2HPO_4 8 mM, KH_2PO_4 1.47 mM and d-glucose 5 mM, pH 7.4 (PBS-g) supplemented with 13 U/ml papain (Sigma), 1 mg/ml bovine serum albumin (Sigma-Aldrich) and 1 mg/ml 1,4-dithiothreitol (Wako Chemicals Co. Ltd., Osaka, Japan). Cells were then dispersed several times with a fire-polished Pasteur pipette and re-suspended in PBS-g and used immediately.

In vitro study

The isolated mouse tracheal epithelial cells were maintained in high glucose Dulbecco's modified Eagle's medium (DMEM, Sigma) supplemented with 10% fetal bovine serum (FBS), 1 U/ml penicillin G, and 0.1 mg/ml streptomycin sulfate, at 37°C, 5% CO_2. The cells were then exposed for 10 min to vehicle, FMS, MWCNT-L, or MWCNT-S in FMS or MWCNT suspensions to a final concentration of 10 μg/ml. Media was then replaced by fresh media. The cells were observed 10 min and 12 and 18 hr after addition of fresh media and the proportion of cells with ciliary movement per total ciliated cells was determined. For each group, approximately 500 cells per dish in three separate dishes were counted.

Rat study

Male Wistar rats aged 6-7 weeks were treated with 0.3 ml of 250 μg/ml MWCNT-L or MWCNT-S (3 rats each) suspended in PF68 vehicle on days 1, 4, and 7. The suspension was administered by a microsprayer (series IA-1B Intratracheal Aerosolizer; Penn-century, Philadelphia, PA, USA) with the tip of the microsprayer just inside the entrance of the trachea (Xu et al., 2012). Administration was done in synchronization with spontaneous inhalation. The rats were sacrificed 24 hr after the last dosing (day 8) under deep anesthesia with isoflurane. The trachea, bronchus and lung were excised and fixed in 4% paraformaldehyde solution. The trachea was transversely cut into 3 pieces, upper, middle and lower parts, and the tracheal sections and the bronchus and lungs were routinely processed for paraffin embedding, sectioning and histological examination.

Histology and Immunostaining

Haematoxylin-Eosin (H&E) stained slides of the trachea; bronchus and lung were examined by board pathologists. The epithelial lesions in each tracheal section were measured with the image analyzing function (Nikon, Tokyo, Japan) and expressed as the ratio of the length of the lesion to the whole length of the tracheal section. The number of granulation foci of the lung sections were counted and expressed as number/cm^2 lung tissue. Localization of MWCNT fibers in the trachea and lung tissue were determined with polarized light microscopy (Olympus BX51N-31P-O, Tokyo, Japan) at × 400 and × 1,000 magnification. Immunostaining of acetyled tublin, a specific marker for cilia, was performed using mouse polyclonal anti-acetyled tublin antibody (Sigma Aldrich). The antibody was diluted 1:1,000 in PBS containing 5% goat albumin and applied to deparaffinized and blocked slides, and the slides were incubated at 4°C overnight. The next day, the slides were washed 3 times in PBS and then incubated for 2 hr with Alexa 488-conjugated goat anti-mouse IgG (Molecular Probe, Eugene, OR, USA) diluted 1:1,000. After washing 3 times in PBS, the slides were counterstained with DAPI (Vector laboratories, Burlingame, CA, USA). Immunostained sections were observed using an A1R laser scanning confocal microscope (Nikon). The ratio of the fluorescent intensity of acetyled tublin in the top layer of cells of the tracheal ciliated epithelium to the fluorescent intensity of DAPI in the underlying submucosal tissue was measured. This ratio was used to compare the intensity of acetyled tublin fluorescence in the different samples. Fluorescence intensity was determined with NIS Elements software (version 3.10; Nikon).

Statistical Analysis

Statistical significance was examined using Tukey's test. P values less than 0.05 were considered to be statistically significant.

RESULTS

In vitro study

Cultures of ciliated cells were incubated in growth media with vehicle (PF68), fluorescent microspheres (FMS), or MWCNT for 10 min. During the 10 min incubation in media containing FMS, FMS in contact with the cilia and/or cell surface could readily be located (white arrow in Fig. 1A in bottom panel), however, 10 min after replacing the FMS containing media with standard growth media, cell-associated FMS could no longer be found. In contrast, ten min after replacing the MWCNT containing media with standard growth media, MWCNT-L and MWCNT-S fibers were not detached from the ciliated cells and could be observed associated with the cilia and/or cell surface (black arrows in Fig. 1A). In the cilia activity test, FMS did not reduce the percentage of cells with active cilia compared to the vehicle group (Fig. 1B). However, the percentage of cells with active cilia in the MWCNT-L treated group was significantly reduced (2.73 ± 1.37; n = 3, $p < 0.05$) compared to the vehicle (18.7 ± 4.28) and FMS (16.57 ± 0.65) groups after 12 hr. Although not significant, a similar decrease was also observed in the MWCNT-S group.

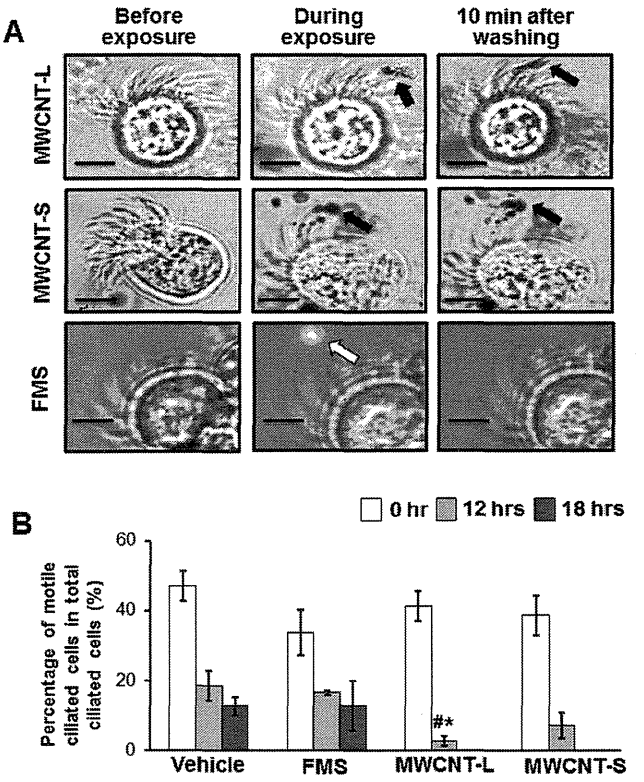

Fig. 1. Exposure of MWCNT to isolated tracheal ciliated cells in vitro. A, Images of ciliated cells exposed to fluorescent microsphere (FMS), MWCNT-L, and MWCNT-S; left, before exposure; middle, during exposure; right, after media change. FMS (white arrow) was clearly removed. MWCNTs were not removed (black arrows). Bars equal 5 μm. B, Percentage of cells with active cilia at time 0 and 12 and 18 hr after media change. n = 3; * $p < 0.05$ vs vehicle control, # $p < 0.05$ vs FMS control.

Rat study

The majority of the epithelium of the trachea is com-

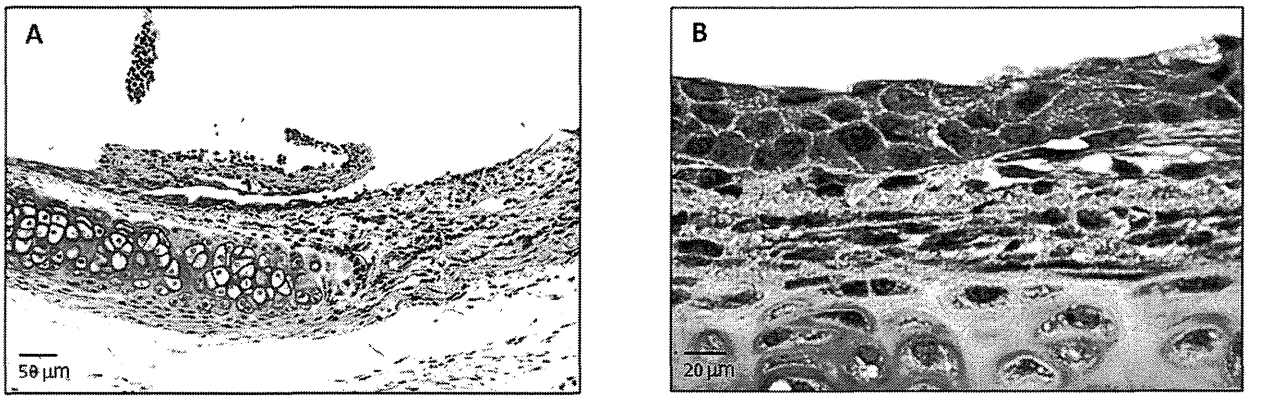

Fig. 2. Erosive lesions and squamous cell metaplasia. A, Representative image showing erosive lesions induced by treatment of MWCNT-L or MWCNT-S; B, Representative image of squamous cell metaplsia.

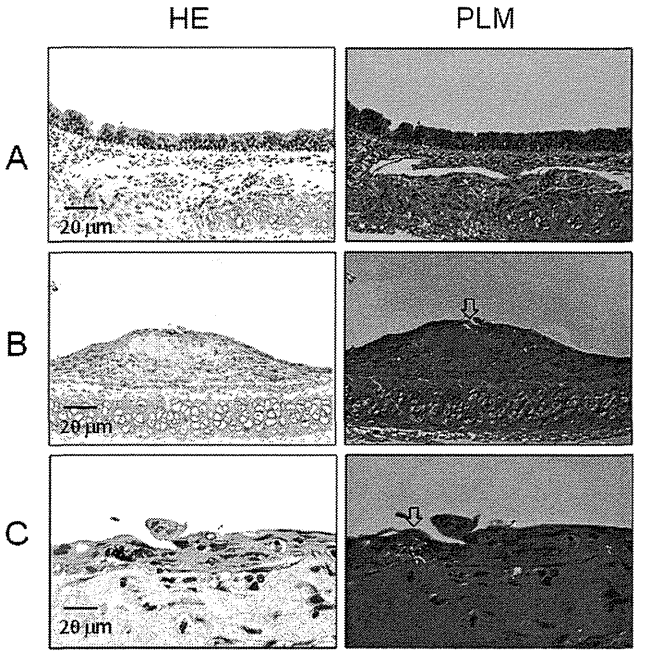

Fig. 3. Tracheal lesions in rat treated with MWCNT-L. A, Undamaged tracheal ciliated epithelium; B, An erosive lesion with granulation tissue underneath the thin regenerating epithelium; C, A higher magnification image of the lesion in B. MWCNT-L fibers (open arrows) can be clearly observed in the granulation tissue by polarized light microscopy (PLM).

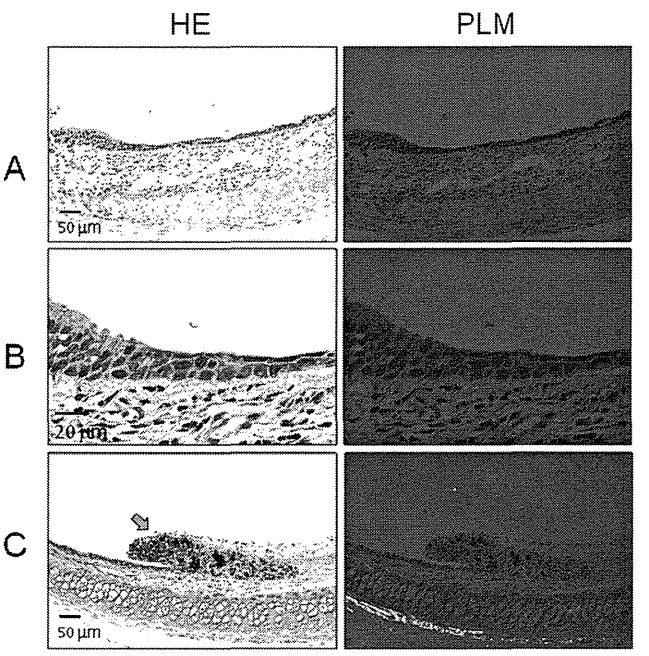

Fig. 4. Tracheal lesions in a rat treated with MWCNT-S. A, Tracheal epithelium showing a transition from undamaged ciliated epithelium to regenerating flat epithelium overlying edematous granulation tissue. B, A higher magnification image of the lesion in B. C, An erosive lesion with granulation tissue containing many black MWCNT-S fibers. MWCNT-S fibers are not visualized by polarized light microscopy (PLM).

posed of a single layer of columnar ciliated cells. Treatment with MWCNT-L induced marked damage to the surface ciliated cells resulting in erosive changes (Fig. 2A) and replacement with flat cells without cilia and occasional squamous cell metaplasia (Fig. 2B). An increase in goblet cells was found in the columnar ciliated cell area, although goblet cell damage was not obvious. MWCNT-L fiber aggregates were frequently observed in the lesions (Figs. 3B and 3C) but not in the healthy mucosa (Fig. 3A). MWCNT-S caused similar mucosal damage (Fig. 4,

Table 1. Lesions in the tracheal epithelium and lung

Treatment	No. of rats	Tracheal epithelium			Lung
		Erosion	Regenerated cells		Granulation tissue (No./cm^2) [b]
		Incidence (%)	Incidence (%)	Proportion [a] (%)	
Vehicle	4	0	0	0	0
MWCNT-L	3	100 ***	100 ***	27.2 ± 8.7**	0.1 ± 0.1
MWCNT-S	4	25 ***	100 ***	32.7 ± 11.5**	1.0 ± 0.2 **,##

Notes: [a], the length of the regenerated lesion compared to the total length of the transverse tracheal circle; [b], the number of granulation lesions per square centimeter of the lung tissue; ** and *** represent p values < 0.01 and 0.001, vs the vehicle; ## represents p values < 0.01, vs MWCNT-L

left panel) but, because of lack of MWCNT-S mediated polarization, the fibers could not be detected by polarized light microscopy (Fig. 4C, right panel).

Table 1 shows the incidences of erosion and incidences and the percentage of the length of the tracheal lesions compared to the total length of the tracheal cross section from rats administered vehicle or MWCNT. Tracheal lesions in rats administered MWCNT-L (27.2 ± 10.5) or MWCNT-S (32.1 ± 15.8) were significantly greater than in rats administered vehicle alone ($p < 0.001$ for both comparisons). Although not significant, the incidences of erosive lesions for MWCNT-L administered rats was greater than for MWCNT-S administered rats.

The ratio of fluorescence of acetyled tublin on the surface of the trachea (0.48 ± 0.06) to submucosal DAPI fluorescence significantly decreased ($p < 0.05$) in rats treated with MWCNT-L (Fig. 5). The value for the MWCNT-S treated rats showed a similar decrease but was not significant. The results clearly indicate the quantitative loss of ciliated cells by treatment with MWCNT-L.

In the lung, granulation foci composed of macrophages and fibrotic cells surrounding MWCNT aggregates was found (Fig. 6). Table 1 shows the number of granulation foci in the lungs of rats administered vehicle or MWCNT. The number of lesions in both the MWCNT-L and MWCNT-S administered groups were significantly higher than in the vehicle control group ($p < 0.001$ for both comparisons). The lesion count in the MWCNT-S group (1.04 ± 0.18) was significantly greater than the MWCNT-L group (0.06 ± 0.06) ($p < 0.05$) (Table 1).

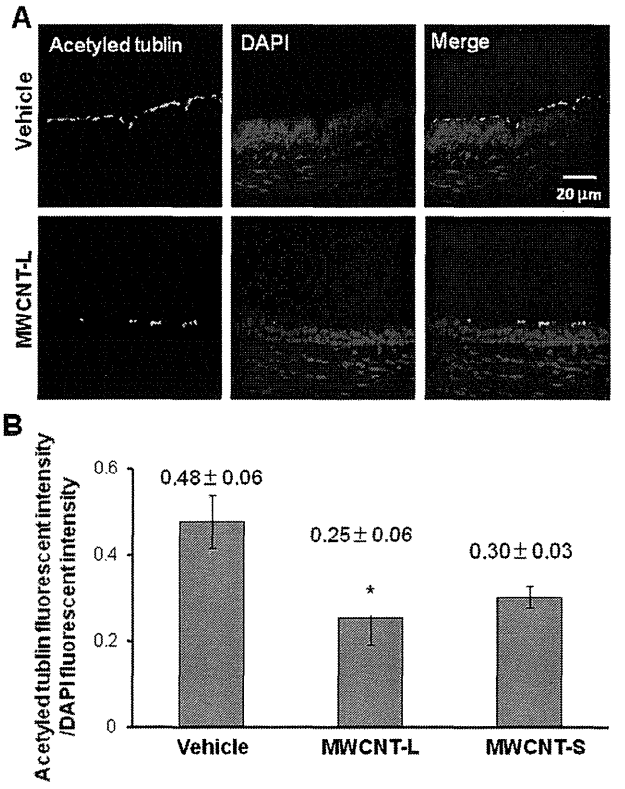

Fig. 5. Decrease in the proportion of ciliated cells in the bronchial epithelium. A, Representative images of immunostaining with anti-acetylated tubulin staining the cilia (left), DAPI (middle) and merged image (right); B, The ratio of the intensity of acetyled tublin to DAPI was decreased in the MWCNT-L group. n = 3~4; * $p < 0.05$ vs the vehicle.

DISCUSSION

The tracheobronchial ciliated epithelium is the first defense line against inhaled dust particles. The dust particles are transported from the lung alveoli through the bronchi and trachea toward the laryngopharynx by its directed ciliary movement. Pathologic changes in the bronchial epithelium such as goblet cell hyperplasia and squamous cell metaplasia have been found by studies

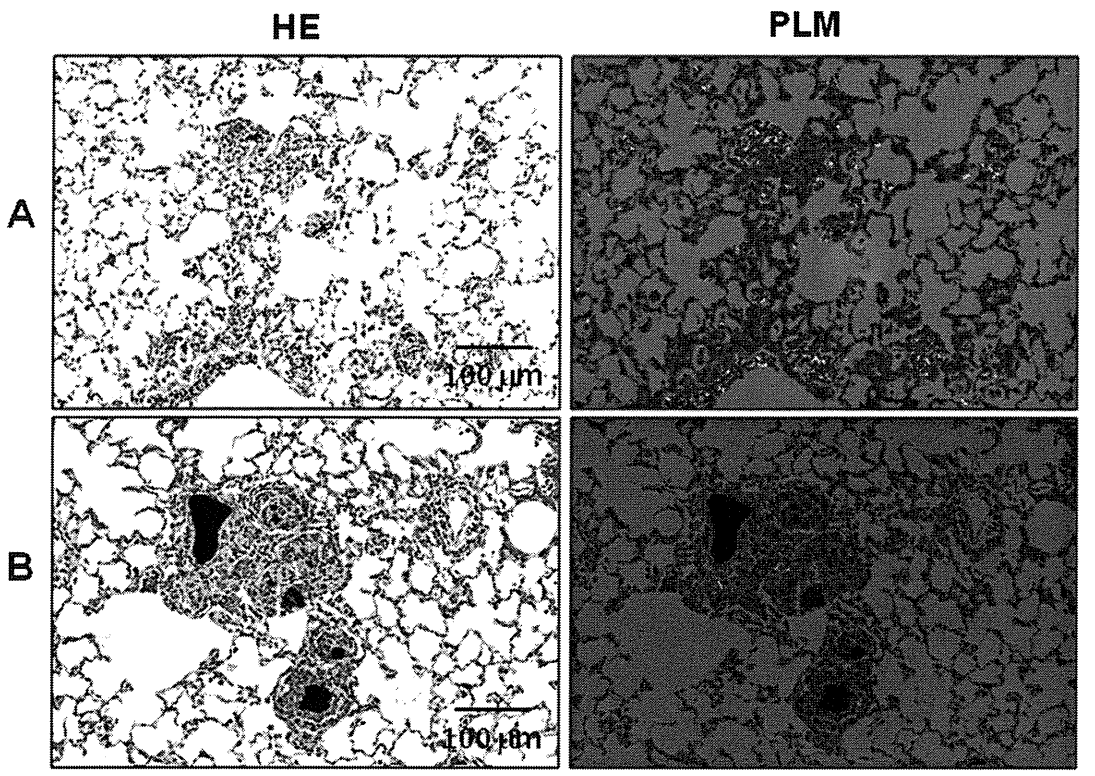

Fig. 6. Demonstration of MWCNTs in the lung tissue. HE and polarized images of the lung tissue treated with MWCNT-L (A) or MWCNT-S (B). Large aggregations of MWNNT-S (black mass) are found encapsulated in granulation tissue and small particles are found in alveolar macrophages. As in the trachea, MWCNT-S is not visualized by polarized light microscopy (PLM).

with particles such as ZnO particles (Choe et al., 1997) and cigarette smoke (Neugut, 1988) and in some disease conditions such as bronchial asthma and chronic bronchitis (Aikawa et al., 1992). The ciliated cell damage in these lesions causes impaired mucociliary protection and increases deposition of particles and microorganisms in the lung, causing inflammatory changes. These alterations may cause chronic injury and cell regeneration leading to an increase in carcinogenesis in the trachea, bronchi and lung.

This is the first report to show that MWCNTs cause extensive damage and loss of ciliated epithelium in the trachea followed by compensatory regeneration of cells without cilia including metaplastic squamous cells. In vitro observation clearly indicated that MWCNT caused impaired function of ciliated cells, potentially resulting in decreased clearance of the fibers from the lung, such as observed in studies of other fibers such as asbestos (Woodworth et al., 1983). Decreased clearance of MWCNT would increase the retention time of the MWCNTs in the trachea and lung, which, in turn, would maintain the toxic effect, leading to even more loss of ciliated cells. This would increase the risk of spread of MWCNT to other organs, especially to the pleural cavity.

It should be noted that damage to the lung differed in MWCNT-L and MWCNT-S administered rats. Inflammatory changes, as evinced by an increase in granulation tissue in the lung, were more extensive in MWCNT-S administered rats. This indicates that there is an organotropic toxic effect of MWCNT. This may be related to their size and shape; however, further studies are necessary to elucidate the mechanism of this difference.

AKNOWLEDGMENTS

This study was supported by Grants-in-Aids by the Ministry of Health, Labour and Welfare, Japan: Risk of Chemical Substance 21340601 (H22-kagaku-ippan-005) and 2524301 (H25-kagaku-ippan-004).

REFERENCES

Aikawa, T., Shimura, S., Sasaki, H., Ebina, M. and Takishima, T. (1992): Marked goblet cell hyperplasia with mucus accumulation in the airways of patients who died of severe acute asthma attack. Chest, 101, 916-921.

Bonner, J.C. (2010): Nanoparticles as a potential cause of pleural and interstitial lung disease. Proc. Am. Thorac. Soc., 7, 138-141.

Cho, W.S., Duffin, R., Howie, S.E., Scotton, C.J., Wallace, W.A., Macnee, W., Bradley, M., Megson, I.L. and Donaldson, K. (2011): Progressive severe lung injury by zinc oxide nanoparticles; the role of Zn2+ dissolution inside lysosomes. Part Fibre. Toxicol., 8, 27.

Choe, N., Tanaka, S., Xia, W., Hemenway, D.R., Roggli, V.L. and Kagan, E. (1997): Pleural macrophage recruitment and activation in asbestos-induced pleural injury. Environ. Health Perspect., 105 Suppl. 5, 1257-1260.

Donaldson, K., Murphy, F.A., Duffin, R. and Poland, C.A. (2010): Asbestos, carbon nanotubes and the pleural mesothelium: a review of the hypothesis regarding the role of long fibre retention in the parietal pleura, inflammation and mesothelioma. Part. Fibre. Toxicol., 7, 5.

Hirano, S., Fujitani, Y., Furuyama, A. and Kanno, S. (2010): Uptake and cytotoxic effects of multi-walled carbon nanotubes in human bronchial epithelial cells. Toxicol. Appl. Pharmacol., 249, 8-15.

Li, J., Kanju, P., Patterson, M., Chew, W.L., Cho, S.H., Gilmour, I., Oliver, T., Yasuda, R., Ghio, A., Simon, S.A. and Liedtke, W. (2011): TRPV4-mediated calcium influx into human bronchial epithelia upon exposure to diesel exhaust particles. Environ. Health Perspect., 119, 784-793.

Lindberg, H.K., Falck, G.C., Suhonen, S., Vippola, M., Vanhala, E., Catalan, J., Savolainen, K. and Norppa, H. (2009): Genotoxicity of nanomaterials: DNA damage and micronuclei induced by carbon nanotubes and graphite nanofibres in human bronchial epithelial cells in vitro. Toxicol. Lett., 186, 166-173.

Ma, W., Korngreen, A., Weil, S., Cohen, E.B., Priel, A., Kuzin, L., and Silberberg, S.D. (2006): Pore properties and pharmacological features of the P2X receptor channel in airway ciliated cells. J. Physiol., 571, 503-517.

Mercer, R.R., Hubbs, A.F., Scabilloni, J.F., Wang, L., Battelli, L.A., Schwegler-Berry, D., Castranova, V. and Porter, D.W. (2010): Distribution and persistence of pleural penetrations by multi-walled carbon nanotubes. Part. Fibre. Toxicol., 7, 28.

Mercer, R.R., Scabilloni, J.F., Hubbs, A.F., Wang, L., Battelli, L.A., McKinney, W., Castranova, V. and Porter, D.W. (2013): Extrapulmonary transport of MWCNT following inhalation exposure. Part. Fibre. Toxicol., 10, 38.

Nagai, H. and Toyokuni, S. (2010): Biopersistent fiber-induced inflammation and carcinogenesis: lessons learned from asbestos toward safety of fibrous nanomaterials. Arch. Biochem. Biophys., 502, 1-7.

Neugut, A.I. (1988): Squamous cell cancers and cigarette smoke: a matter of exposure. Med. Hypotheses., 26, 9-10.

Rotoli, B.M., Bussolati, O., Bianchi, M.G., Barilli, A., Balasubramanian, C., Bellucci, S. and Bergamaschi, E. (2008). Non-functionalized multi-walled carbon nanotubes alter the paracellular permeability of human airway epithelial cells. Toxicol. Lett., 178, 95-102.

Simet, S.M., Sisson, J.H., Pavlik, J.A., Devasure, J.M., Boyer, C., Liu, X., Kawasaki, S., Sharp, J.G., Rennard, S.I. and Wyatt, T.A. (2010): Long-term cigarette smoke exposure in a mouse model of ciliated epithelial cell function. Am. J. Respir. Cell. Mol. Biol., 43, 635-640.

Woodworth, C.D., Mossman, B.T. and Craighead, J.E. (1983): Squamous metaplasia of the respiratory tract. Possible pathogenic role in asbestos-associated bronchogenic carcinoma. Laboratory investigation; a journal of technical methods and pathology, 48, 578-584.

Xu, J., Futakuchi, M., Alexander, D.B., Fukamachi, K., Numano, T., Suzui, M., Shimizu, H., Omori, T., Kanno, J., Hirose, A. and Tsuda, H. (2014): Nanosized zinc oxide particles do not promote DHPN-induced lung carcinogenesis but cause reversible epithelial hyperplasia of terminal bronchioles. Arch. Toxicol., 88, 65-75.

Xu, J., Futakuchi, M., Shimizu, H., Alexander, D.B., Yanagihara, K., Fukamachi, K., Suzui, M., Kanno, J., Hirose, A., Ogata, A., Sakamoto, Y., Nakae, D., Omori, T. and Tsuda, H. (2012): Multi-walled carbon nanotubes translocate into the pleural cavity and induce visceral mesothelial proliferation in rats. Cancer Sci., 103, 2045-2050.

A Novel Transgenic Mouse Model Carrying Human Tribbles Related Protein 3 (TRB3) Gene and Its Site Specific Phenotype

Yuto Sakai,[a,b] Katsumi Fukamachi,[b] Mitsuru Futakuchi,[b] Ichiro Miyoshi,[c] Hiroyuki Tsuda,[d] Masumi Suzui,*[,b] and Hidetoshi Hayashi*[,a]

[a] *Department of Drug Metabolism and Disposition, Graduate School of Pharmaceutical Sciences, Nagoya City University;* [d] *Nanomaterial Toxicology Project, Nagoya City University; 3–1 Tanabe-dori, Mizuho-ku, Nagoya 467–8603, Japan:* [b] *Department of Molecular Toxicology, Graduate School of Medical Sciences and Medical School, Nagoya City University; and* [c] *Department of Comparative and Experimental Medicine, Graduate School of Medical Sciences and Medical School, Nagoya City University; 1 Kawasumi, Mizuho-cho, Mizuho-ku, Nagoya 467–8601, Japan.*

Received March 24, 2014; accepted March 31, 2014

Tribbles related protein 3 (TRB3) pseudokinase plays a crucial role in cell proliferation, migration and morphogenesis during development. In our recent study, an introduction of human TRB3 gene into mouse mammary tumor cells caused an increase of proliferation of tumor cells and their nuclear size. In the current study, to examine whether this gene causes *de novo* morphological changes in a specific organ site we have developed a novel variation of the transgenic mouse model that conditionally expresses human TRB3 (hTRB3) gene using Cre-recombinase (Cre)/loxP recombination system. By injecting hTRB3 transgene construct into pronuclei of mouse embryo, we eventually obtained four hTRB3 mice. The gene expression was controlled by infection of adenovirus-expressing Cre *via* the tail vein of hTRB3 mouse. In Cre-mediated hTRB3 mouse, expression of the hTRB3 protein was detected in the cytoplasm of hepatocytes in the liver. Expression of this protein was also seen in lymphocytes in the spleen, glomerular endothelial cells, and epithelial cells of collecting duct of the kidney. In hepatocytes of the hTRB3 mouse, nuclear size was significantly greater than that of the wild type mouse, indicating that hTRB3 can play a role at least in part in hepatic morphogenesis. The present animal model may provide a system for evaluation of *de novo* morphological changes induced by a specific transgene in a specific organ site.

Key words Tribbles related protein 3 (TRB3); transgenic mouse; Cre-recombinase (Cre)/loxP

Tribbles related protein 3 (TRB3) is one of the mammalian homologues of *Drosophila* Tribbles. This molecule contains a serine/threonine kinase catalytic domain but lacks an ATP binding site or one of the conserved catalytic motifs essential for kinase activity.[1–3] TRB3 has also been shown to be involved in multiple cellular processes such as glucose/lipid metabolism, muscle/adipocyte differentiation, and stress response by interacting with various functional proteins.[1,3–10] Three mammalian Tribbles homologues, TRB1, TRB2, and TRB3 are crucial modulators of tumorigenesis.[3,11–13] TRB1 and TRB2 induce acute myelogenous leukemia by inhibiting CCAAT/enhancer binding protein α (C/EBPα) function.[12] TRB3 is highly expressed in a wide range of human carcinoma cell lines and in several types of human carcinoma.[3,13] We have recently demonstrated that TRB3 promotes proliferation and induces polyploidy of mouse mammary tumor cells.[14] This finding was likely to indicate TRB3's response to morphological function. In the current study, by utilizing the recombinant adenovirus expressing Cre-recombinase (Cre) system we examined whether human TRB3 gene causes *de novo* morphological changes in a specific organ site.

MATERIALS AND METHODS

Generation of Human TRB3 Transgenic Mouse We ligated flag-tagged full length human TRB3 (hTRB3) cDNA[7] into *Kpn*I and *Swa*I restriction sites of pCALNL5 vector (DNA Bank, RIKEN Bio Resource Center, Ibaraki, Japan),[15–17] and this construct was termed pCALNL-flag-hTRB3. The pCALNL-flag-hTRB3 was digested at *Ssp*I/*Hin*dIII restriction sites.

African green monkey kidney fibroblast cell line COS7 was obtained from Cell Resource Center for Biomedical Research Institute of Development, Aging and Cancer, Tohoku University, Sendai, Japan and cultured in Dulbecco's modified Eagle's medium (DMEM) (Wako Pure Chemical Industries, Ltd., Osaka, Japan) containing 10% fetal bovine serum (FBS) (Life Technologies, Inc., Rockville, MD, U.S.A.). Expression vectors pCALNL-flag-hTRB3 (generated in this study), pcDNA3.1-flag-hTRB3 (used as positive control),[7] pxCANCre (DNA Bank, RIKEN Bio Resource Center) and empty vector pCALNL5 (used as negative control) were transfected into COS7 cells using FuGENE6 reagent (Roche Diagnostics Corp., Indianapolis, IN, U.S.A.), and these cells were cultured in in a 6-cm culture dish. Using the transfected cells, levels of protein expression were confirmed by Western blot assays.

After confirming the Cre/loxP system functions by examining the expression status of hTRB3 that can be measured with Flag expression, the purified cassette (Fig. 1) was injected into the pronuclei of C57BL/6NCrSlc mouse (CLEA Japan, Tokyo, Japan). A total of 184 injected eggs were transplanted into pseudo-pregnant C57BL/6NCrSlc mouse. Of 8 potential transgenic mice screened, four mice were shown to carry the transgene by polymerase chain reaction (PCR) as described below. These four transgenic founder mice were then mated with wild type C57BL/6NCrSlc mice (wild mice) and offspring were screened for the presence of the transgene by PCR assay of genomic DNA isolated from tail

The authors declare no conflict of interest.

* To whom correspondence should be addressed. e-mail: suzui@med.nagoya-cu.ac.jp; hhayashi@phar.nagoya-cu.ac.jp

© 2014 The Pharmaceutical Society of Japan

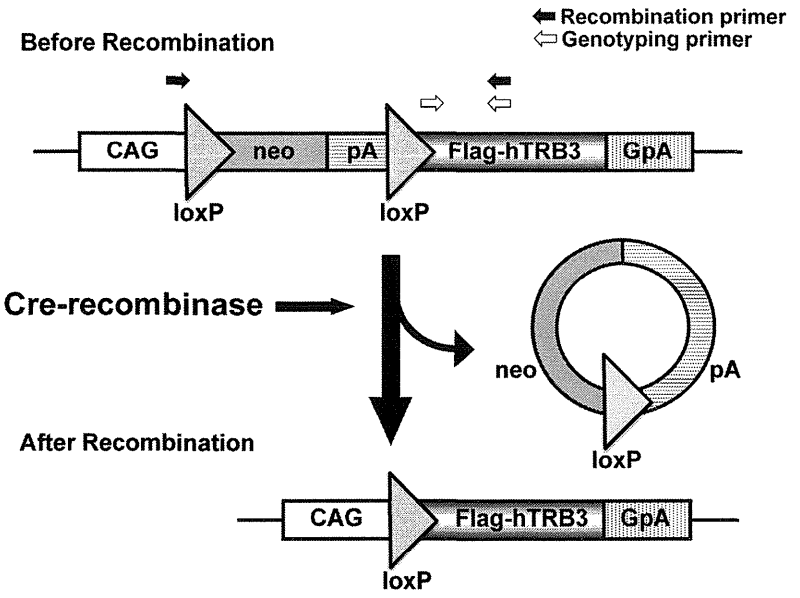

Fig. 1. Scheme of Recombination of hTRB3 Construct

The pCALNL-flag-hTRB3 construct is comprised of a hybrid CMV enhancer/chicken β-actin (CAG) promoter, a cassette for the neomycin resistance gene flanked by loxP sites, and a sequence containing a human TRB3 with a Flag-tag. Infection with the Cre expressing adenovirus results in recombination of hTRB3 construct, eventually generating a functional flag-hTRB3 gene expression unit. GpA, rabbit β-globin poly A site; pA, SV40 early poly A site.

biopsies at the age of 3 weeks. The following primers were used: geno-hTRB3F (5′-TGTCTGGATCAAATCCGAAC-3′) and geno-hTRB3R (5′-ATCCGTCGACCCTTGTCATC-3′). In the present study, we used these transgenic mice termed NCrSlcBL6-TgN(hTRB3) mice (hTRB3 mice). The mouse was maintained in plastic cages in an airconditioned room with a 12 h light/12 h dark cycle.

hTRB3 mouse embryonic fibroblast cell line (hTRB3 MEF) that carries human TRB3 gene was generated from hTRB3 mouse. MEF cell line was also generated from wild mouse. The hTRB3 female mouse was euthanized at 14 d postcoitum and embryos were removed from placenta. After excising head and viscera, the embryo was cut into small pieces until it became possible to pipette. One milliliter of trypsin/EDTA (Life Technologies) was added to one embryo and incubated at 37°C for 15 min. After adding DMEM containing 10% FBS, centrifugation was done and supernatant containing MEF cells was used for cell culture. MEF cell lines were cultured in DMEM containing 10% FBS.

To see whether the Cre/loxP system properly functions, we examined the expression status of mRNA and protein of hTRB3 in MEF cells. Adenovirus carrying the Cre gene (AxCANCre) was prepared as described previously.[15,16] **Adenovirus vectors were amplified in HEK-293 cell line that** was purchased from ATCC (Manassas, VA, U.S.A.), cultured **in DMEM containing 10% FBS, and purified using Vivapure** Adenopack (Vivascience, Hannover, Germany). The titer of the adenovirus was determined by using the Rapid titer kit (Clontech, Mountain View, CA, U.S.A.). The virus stock was concentrated to 1.0×10^{10} pfu per mL. MEF cells with or without hTRB3 transgene were infected with Cre expressing adenovirus (0, 100, 200 multiplicity of infection (MOI)) for 2 h. After the infection, cells were cultured in DMEM containing 10% FBS for 48 h, genomic DNA, total RNA, and protein were extracted and used for PCR, reverse transcription (RT)-PCR, and Western blot assays.

After confirming that the Cre/loxP system functions *in vitro*, the system was introduced into mice and initiated by infecting animals with Cre expressing adenovirus. Cre expressing adenovirus (1×10^8 pfu/mouse) was injected into the tail vein of 4-week-old mouse. To induce Flag-tagged-human TRB3 gene, adenovirus in which the expression of Cre was under the control of the CAG promoter was used. Ten days after Cre expressing adenovirus was injected, all mice were euthanized and complete autopsy was done. Liver, spleen, and kidneys were carefully removed and processed for macroscopic examination and histopathological/immunohistochemical analyses. All experimental procedures conformed to the Regulations for Animal Experimentation at Nagoya City University were reviewed by the Institutional Laboratory Animal Care **and Use Committee of Nagoya City University and finally approved** by the President of University.

Immunohistochemical Analysis These assays were performed using an established method as described elsewhere.[18] **Three-micrometer-thick paraffin sections were prepared from** liver, spleen and kidney. These sections were treated in 3% H_2O_2 for 10 min to block the endogenous peroxidase activity. For antigen retrieval, the sections were brought to boiling in 0.1 M citrate buffer, pH 6.0. Sections were then incubated with a primary antibody (1 : 500 dilution) of the FLAG (Sigma, St. Louis, MO, U.S.A.) at room temperature for 1 h. After incubation with secondary antibody, sections were then stained using an ABC kit (Vector Laboratories Inc., Burlingame, CA, U.S.A.) **according to the manufacturer's instructions. The** number of Cre-treated wild mouse was one, and that of Cre-treated hTRB3 mice was eight. The number of untreated wild mouse was one and that of untreated hTRB3 mouse was also one. Each liver slide has two to four tissue slices. In the liver tissue slices of hTRB3 and wild mice, the longest diameter of nucleus of the liver cell was determined by image analysis (Olympus DP70 system, Olympus Corp., Tokyo, Japan). Four **high power fields per liver tissue were examined and more** than 100 nuclei were counted in each liver tissue.

RT-PCR and PCR Assays These assays were done with

established procedures.[18] Total RNA was extracted from each cell line grown in 9-cm culture dishes using ISOGEN (Nippon Gene, Toyama, Japan). The reaction mixture contains 4 μg of total RNA, 1 μL of 10 mM deoxyribonucleotide triphosphate (dNTP) (Life Technologies), 1 μL of Random primers (Life Technologies) and 7 μL of distilled water. The reaction mixture was then incubated at 65°C (5 min) for denaturation, chilled on ice for 1 min and added 4 μL of 5×RT buffer (Life Technologies), 1 μL of 0.1 M dithiothreitol (DTT), 1 μL of the RNase out (Life Technologies) and 1 μL of Superscript III Reverse Transcriptase (Life Technologies). After the addition of these reagents, the reaction mixture was incubated at 50°C (1 h) for random primer annealing and 70°C (15 min) for cDNA preparation. One microliter of the reaction mixture was then used for PCR. The genomic DNA was isolated from MEF cells that were derived from hTRB3 and wild mice. The primer sequences of PCR analysis used in this study were as follows: human TRB3-specific primer set, hTRB3F (5′-CAA GTC GCT CTG AAG GTT CC-3′) and hTRB3R (5′-CCA TCC TAC TCT GGC AAA GC-3′), Cre/loxP recombination primer set, CAGpF (5′-CGT GCT GGT TGT TGT GCT GTC T-3′), and geno-hTRB3R (5′-ATC CGT CGA CCC TTG TCA TC-3′). β-Actin-specific DNA fragments from the same RNA samples were amplified and served as internal controls. Primers actin F (5′-CCG TAA AGA CCT CTA TGC CAA CA-3′) and actin R (5′-CGG ACT CAT CGT ACT CCT GCT T-3′) were used for amplification of β-actin. Interleukin-2 (IL-2)-specific DNA fragments from genomic DNA samples were also amplified and served as internal controls. Primers IL-2 F (5′-CTA GGC CAC AGA ATT GAA AGA TCT-3′) and IL-2 R (5′-GTA GGT GGA AAT TCT AGC ATC ATC C-3′) were used for amplification of IL-2. PCR was conducted for 26–30 cycles in an iCycler (Bio-Rad Laboratories, Inc., Hercules, CA, U.S.A.). Each amplification cycle consisted of at 94°C (0.5 min) for denaturation, 60°C (0.5 min) for primer annealing, and 72°C (1 min) for extension. After PCR amplification, the DNA fragments were stained with ethidium bromide and analyzed by 2% agarose gel electrophoresis. The results were confirmed by repeating experiments.

Western Blot Assays These assays were done with established procedures.[19] The cells were lysed in radioimmunoprecipitation assay (RIPA) buffer (50 mM Tris–HCl (pH 8.0), 150 mM NaCl, 0.1% sodium dodecyl sulfate (SDS), 0.5% deoxycholate, and 1% Triton X-100). The lysates were subjected to SDS-polyacrylamide gel electrophoresis (PAGE) (12.5%), transferred onto a polyvinylidene difluoride (PVDF) membrane (Immobilon P, Millipore Corp., Bedford, MA, U.S.A.) and probed with the antibodies. The primary antibodies used in the present study were anti-β-actin monoclonal antibody (AC-15, Sigma, St. Louis, MO, U.S.A.) and anti-FLAG monoclonal antibody (M2, Sigma, St. Louis, MO, U.S.A.). The antiserum against human TRB3 was prepared as described previously.[7] Proteins of interest were visualized using immunoStar Zeta (Wako) and light emission was quantified with a Light-capture (ATTO Corp., Tokyo, Japan). Each assay was repeated more than three times to confirm the results.

Statistical Analysis Differences in the mean diameter of the nucleus of the liver cells between hTRB3 and wild type mice were analyzed by Student's or Welch's t-test. The value of $p<0.05$ was considered to be significant.

RESULTS AND DISCUSSION

We have developed a novel variation of the transgenic mouse model by using Cre/loxP system to express TRB3 protein in the liver, spleen, and kidney tissues. Mean diameter of nucleus was greater in hepatic cells transfected with hTRB3 than non-transfected hepatocytes. This morphological difference depending on transfection status is in accordance with our recent experiments demonstrating that hTRB3 transfected mouse mammary tumor cells exhibited enlarged nuclear size and that *TRB3* gene promotes cell proliferation and chromosomal instability by causing polyproidization during development of mouse mammary tumor.[14] Taken together, *hTRB3* gene may influence its response to morphological function and the present animal model system would be useful to see if this gene causes *de novo* morphological changes leading to tumorigenesis in a specific organ site.

Conditional Expression of Human TRB3 (hTRB3) Transgene Was Controlled by Cre-Recombinase The system was originated by investigators.[15,20] This system is a powerful on/off switching tool when timed/tissue specific expression of gene is critical in cultured cells or transgenic animals. This system can also be used in experiments of developmental processes involving proteins that are suspected of exerting different functions in embryogenesis and in adult animals and that are lethal if the gene is expressed in the embryo. In the present study, little was known about the lethality when hTRB3 gene was introduced into mouse embryo. Thus, we selected this Cre/loxP system to avoid the issue of embryonic lethal.

In Fig. 2 panel A, lysate sample in lane 1 was derived from COS7 cells that were transfected with both hTRB3 transgene construct (pCALNL-flag-hTRB3) and Cre expression vector (pxCANCre). Lysate samples of lanes 4 and 5 were negative and positive controls, respectively. When COS7 cell were transfected with both hTRB3 transgene construct and Cre expression vector, the FLAG expression was present (lane 1) as seen in the positive control (lane 5). Negative and positive controls (lanes 4 and 5) consisted of COS7 cells transfected with empty vector (pCALNL5) and hTRB3 expression vector (pcDNA3.1-flag-hTRB3), respectively. These findings indicate that expression of hTRB3 transgene was controlled by the Cre/loxP system. This hTRB3 construct was used for injection as described below.

Generation of hTRB3 Transgenic Mouse Wagner *et al.* previously reported that the ratio of the number of offspring/embryos to foster mother was 23%.[21] The ratio of the number of mouse that expresses transgene/the number of offspring was 10–40%.[22]

In the present Cre/loxP system, the ratio of the number of mouse expressing transgene/embryos to foster mother was 4/184=2%. After infection of Cre, this enzyme excises the stuffer DNA region loxP–*neo*-poly A–loxP (Fig. 1). This step initiates gene expression of hTRB3. By introducing hTRB3 transgene construct (Fig. 1) into pronuclei of mouse embryo, four hTRB3 mice were eventually obtained (Fig. 2 panel B). These four hTRB3 mice were mated with wild mice and offspring were produced. hTRB3 genotyping was done using genomic DNA derived from the offspring, and most of them carried hTRB3 (Fig. 2 panel C). In three of four mice, hTRB3 gene was transmitted to next generation.

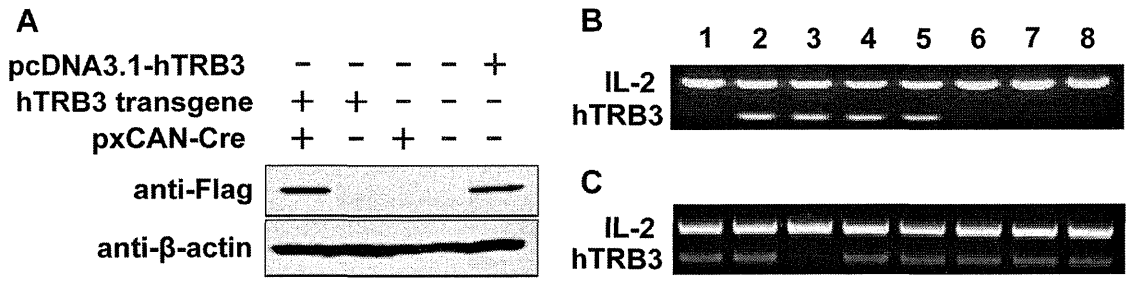

Fig. 2. Confirmation of hTRB3 Protein Expression and Detection of hTRB3 DNA Fragment

(A) Conditional expression of hTRB3. Lysate sample in lane 1 was derived from COS7 cells that were transfected with both hTRB3 construct (pCALNL-flag-hTRB3) and Cre expression vector (pxCANCre). Lysate samples of lanes 2 and 3 consisted of COS7 cells transfected with hTRB3 construct and Cre expression vector, respectively. Lysate samples of lanes 4 and 5 were negative and positive controls, respectively. Negative and positive controls (lanes 4 and 5) consisted of COS7 cells transfected with empty vector (pCALNL5) and hTRB3 expression vector (pcDNA3.1-flag-hTRB3), respectively. The FLAG expression was present (lane 1) as seen in the positive control (lane 5). (B, C) Detection of hTRB3 DNA fragments by PCR assay. We used hTRB3 transgenic mice (hTRB3 mice) as described in Materials and Methods. Genomic DNA was extracted from mice tails and used for amplification of hTRB3 and IL-2 DNA fragments. (B) hTRB3 DNA fragment was seen in 4 mice of 8 potential transgenic mice. The number indicates the individual mouse number. (C) hTRB3 DNA fragment was seen in 7 of 8 offspring generated by mating hTRB3 mice with wild mice.

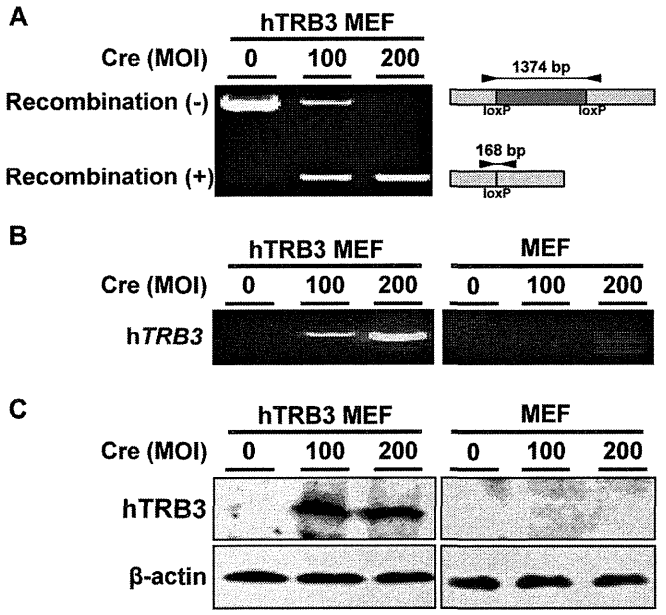

Fig. 3. Confirmation of Recombination of hTRB3 Construct and hTRB3 mRNA/Protein Expression in hTRB3 MEF Cells

hTRB3 MEF and MEF cells were generated from hTRB3 and wild mice, respectivly. These cells were treated with Cre expressing adenovirus (0, 100, 200 MOI). MOI indicates multiplicity of infection. (A) Confirmation of recombination of hTRB3 construct in hTRB3 MEF cells by PCR assay. A 168-bp DNA fragment derived from recombinant hTRB3 construct was seen in cells treated with Cre expressing adenovirus. hTRB3 DNA fragments were not PCR-amplified in MEF cells (data not shown). (B) Confirmation of hTRB3 mRNA expression in hTRB3 MEF/MEF cells by RT-PCR assay. Increasing mRNA expression was seen in hTRB3 MEF cells (left panel). No mRNA expression was seen in MEF cells (right panel). (C) Confirmation of hTRB3 protein expression by Western blot assay. hTRB3 protein expression was observed in hTRB3 MEF cells but not in MEF cells. β-Actin was used as an internal control.

To confirm whether Cre-mediated recombination of the transgene occurs in MEF cells, we examined the existence of DNA fragment consisting of hTRB3 construct by PCR assay. hTRB3 MEF cells and MEF cells were generated from 14-d-old embryos of hTRB3 and wild mice, respectively. Cells were then infected with Cre expressing adenovirus as described in Materials and Methods. A 168-bp DNA fragment was seen when the recombination occurred (Fig. 3 panel A). However, a longer 1374-bp DNA fragment was seen unless hTRB3 MEF cells were treated with Cre expressing adenovirus, indicating no recombination of the transgene. We also examined the mRNA/protein expression status of hTRB3 by RT-PCR/Western blot assays. There was a marked mRNA/protein expression of hTRB3 in hTRB3 MEF cells treated with Cre (Fig. 3, panels B left and C left). There was no expression seen in MEF cells that were treated with Cre (Fig. 3, panels B right and C right).

hTRB3 Protein Is Expressed in Liver, Spleen and Kidney Tissues, and hTRB3 Gene Affects the Nuclear Size in the Liver Cell To examine whether *hTRB3* gene causes *de novo* morphological changes leading to tumorigenesis in a specific organ site, we performed immunohistochemical analysis and hematoxylin/eosin staining for histopathological examination in liver, spleen, and kidneys of the hTRB3 mouse. There were no apparent abnormalities seen in morphology and behavior in either hTRB3 or wild mice. As shown in Fig. 4, hTRB3 and wild mice, both of which were not infected with Cre expressing adenovirus, exhibited no significant histopathological differences in the liver (Figs. 4A, D), spleen (Figs. 4B, E), and kidney (Figs. 4C, F) tissues. There were also no apparent histopathological differences in the spleen and kidney tissues between hTRB3 and wild mice, both of which were infected with Cre expressing adenovirus (Figs. 5B, E, and Figs. 5C, F). In the hTRB3 mouse that infected with Cre expressing adenovirus, approximately 20% of hepatocyets exhibited positive cytoplasmic staining of FLAG, indicating hTRB3 protein was expressed in these hepatocytes (Fig. 6A, arrow), whereas the remaining 80% stained faintly or uncertainly. Positive FLAG staining was also seen in sinusoid in liver tissue (Fig. 6A arrowhead). In the spleen of the hTRB3 mice, approximately 10% of lymphocytes were positively stained with FLAG (Fig. 6B). In the kidney of the hTRB3 mice, approximately 20% of epithelial cells of the tubules and collecting duct were positively stained with FLAG (Fig. 6C). Also, endothelial cells of capillaries of glomeruli were positive (Fig. 6D). Perivascular inflammation in liver tissue was also seen in the hTRB3 mouse (Fig. 5A). In liver cells of the hTRB3 mouse, the mean longest diameter of nucleus was significantly greater than that of the wild mice (9.4 ± 0.19 *versus* 6.3 ± 0.11 μm, $p<0.001$) (Fig. 5A *versus* 5D). These results indicate that the Cre/loxP recombination system functions at least in part in liver, spleen, and kidney of the C57BL/6NCrSlc mouse, and that hTRB3 gene causes morphological changes in nuclear size of hepatocytes. An increase in nuclear size occurred in both FLAG-positive

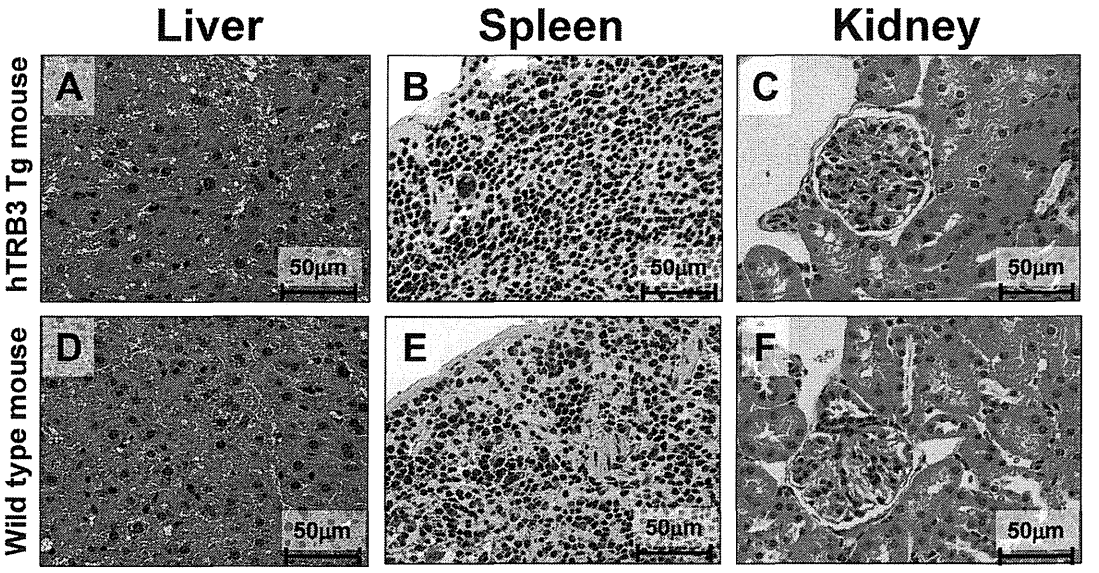

Fig. 4. Representative Histological Features of the Liver, Spleen, and Kidney Tissues of hTRB3 and Wild Mice without Cre Treatment

Note that no apparent histological differences were observed between hTRB3 (A–C) and wild (D–F) mice, both of which were not introduced hTRB3 transgene. Magnification was ×400 in all six images.

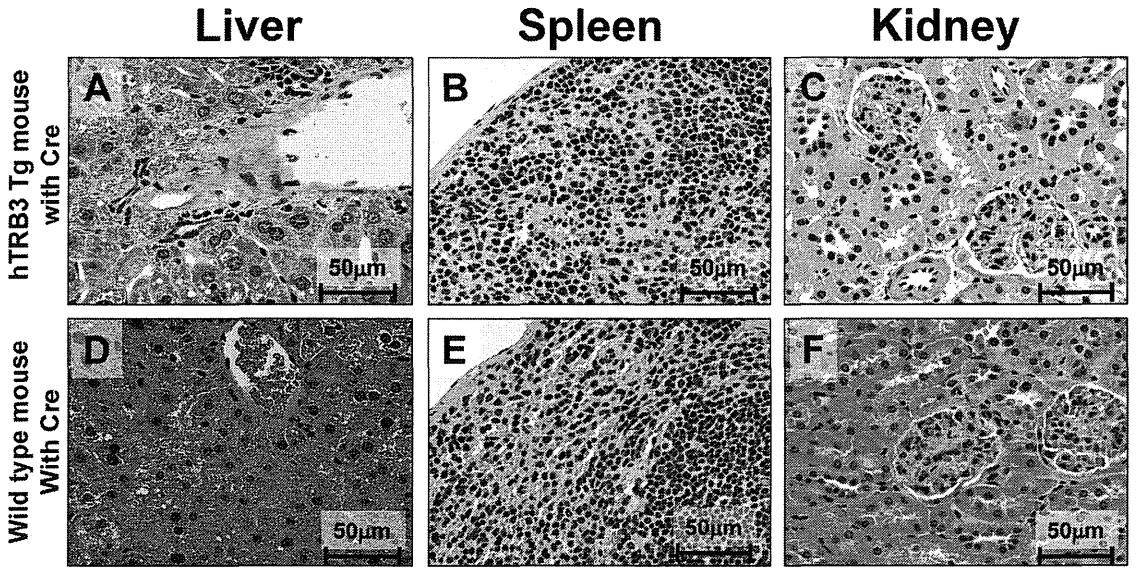

Fig. 5. Representative Histological Features of the Liver, Spleen, and Kidney Tissues of hTRB3 and Wild Mice with Cre Treatment

hTRB3 and wild mice were infected with Cre expressing adenovirus and HE staining was conducted with liver, spleen and kidney tissues derived from hTRB3 mouse (A–C) or wild mouse (D–F). No apparent abnormality was seen in liver tissue derived from wild mouse (B). Note that nuclear size of hepatocyte in the liver tissue derived from hTRB3 mouse increases compared to that of wild mouse (A). Slight perivascular inflammation is also seen (A). Note that no apparent histological differences in spleen or kidney tissues were observed between hTRB3 (B, C) and wild (E, F) mice. Magnification was ×400 in all six images.

and negative hepatocytes (Figs. 5A, D). This is presumably because endogenous TRB3 in mouse hepatocytes may function as exogenous hTRB3 simultaneously does. Indeed, in a recent experiment we found that both endogenous and exogenous TRB3 express in a cell line that stably expresses exogenous TRB3 gene.[14] Further, Bowers *et al.* postulate that there is a feedback response of TRB3 protein accumulation activating a higher expression of TRB3 transcript.[3]

We first estimated that Cre-mediated recombination of the transgene had occurred more than 50% in frequency. Anton *et al.* also estimated approximately 50% of Cre-dependent recombination *in vitro*.[20] Kudoh *et al.* developed a mouse model for Duchenne muscular dystrophy using a Cre/loxP recombination system, and the ratio of the number of 100% chimeras/the number of embryo transplanted ranged from zero to 5%.[23] In our experiment, actual efficiency of the present system resulted in 20%. Differences in experimental systems (*i.e.*, *in vitro*/*in vivo*, animal strain used in the experiment, sequence of the restrictive target sites, and MOI) may explain discrepancies reported on efficiency of recombination. It may be possible for us to improve on this efficiency by optimizing MOI values or the timing of adenovirus infection.

Commonly used adenoviruses derived from human serotype 2 (Ad2) and 5 (Ad5) infect a broad range of organ tissues through interaction with the 46-kDa coxackie and adenovirus receptor (CAR).[24] The major issue for successful site specific transgene delivery is tissue selectivity. Systemically injected adenovirus into mice primarily localize to hepatocytes with

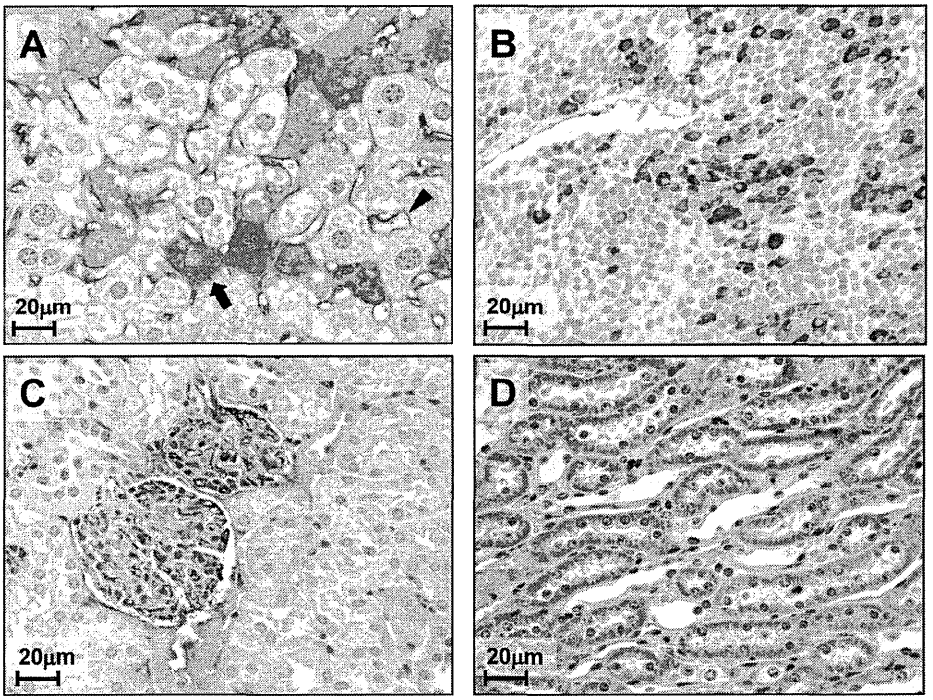

Fig. 6. Representative Immunohistochemical Analysis of Liver, Spleen and Kidney Tissues of hTRB3 and Wild Mice with Cre Treatment

hTRB3 and wild mice were infected with Cre expressing adenovirus and immunohistochemical staining of liver (A), spleen (B) and kidney (C, D) tissues derived from hTRB3 mouse were done. (A) Immunohistochemical staining of liver tissue derived from hTRB3 mouse. Note that FLAG-mediated hTRB3 protein expression was seen in the cytoplasmic region of hepatocytes (arrow) and sinusoid of the liver tissue (arrowhead). FLAG-mediated hTRB3 protein expression was faintly or uncertainly stained in the remaining hepatocytes. (B) FLAG-mediated hTRB3 protein expression was seen in lymphocytes of spleen tissue. (C) In the kidney tissue of the hTRB3 mouse, hTRB3 was positively stained in epithelial cells of the tubules and collecting duct. (D) hTRB3 was also positively stained in endothelial cells of the capillary of glomeruli of the kidney. Magnification was ×400 in all six images.

consequent hepatotoxicity.[24–26] In the present study, we used adenovirus vector Ad5 and FLAG-mediated expression of hTRB3 transgene was seen in three organs such as liver, spleen, and kidneys, indicating low tissue selectivity.

In the hTRB3 mice, we found that nuclear diameter of FLAG-stained hepatocytes was significantly greater than that of wild mice. Some investigators report an increase in nuclear size as the disorder progresses from normal to carcinoma.[27,28] Furthermore, nuclear size increases monotonically with nuclear DNA content.[29] The findings in the present study together with our recent experiment[14] indicate that TRB3 affects nuclear size of hepatocytes that were infected with Ad5. There are several documents demonstrating morphological changes and hepatocarcinogenesis. Large cell change of hepatocytes was regarded as a precancerous lesion.[30] Nuclear enlargement of hepatocytes was induced by the treatment of animals with carcinogen.[31–33] Of these reports, Clawson *et al.* found that hepatocarcinogen induced nuclear enlargement is associated with substantial diploid to tetraploid shifts in hapatocytes.[31] Regarding TRB3's function, it is reported that TRB3 accumulates in response to fasting and inhibits the activation of the kinase Akt in the liver.[1,34] TRB3 also stimulates lipolysis by triggering the degradation of acetyl-coenzyme A carboxylase (ACC) in adipose tissue.[10]

Acknowledgments We thank Tomomi Miyamoto for excellent technical support on the production of transgenic mice. This study was supported by Grants-in-Aid from the Ministry of Education, Culture, Sports, Science and Technology of Japan and the Ministry of Health, Labour, and Welfare of Japan.

REFERENCES

1) Du K, Herzig S, Kulkarni RN, Montminy M. TRB3: a tribbles homolog that inhibits Akt/PKB activation by insulin in liver. *Science*, **300**, 1574–1577 (2003).
2) Wilkin F, Suarez-Huerta N, Robaye B, Peetermans J, Libert F, Dumont JE, Maenhaut C. Characterization of a phosphoprotein whose mRNA is regulated by the mitogenic pathways in dog thyroid cells. *Eur. J. Biochem.*, **248**, 660–668 (1997).
3) Bowers AJ, Scully S, Boylan JF. SKIP3, a novel *Drosophila* tribbles ortholog, is overexpressed in human tumors and is regulated by hypoxia. *Oncogene*, **22**, 2823–2835 (2003).
4) Kato S, Du K. TRB3 modulates C2C12 differentiation by interfering with Akt activation. *Biochem. Biophys. Res. Commun.*, **353**, 933–938 (2007).
5) Kiss-Toth E, Bagstaff SM, Sung HY, Jozsa V, Dempsey C, Caunt JC, Oxley KM, Wyllie DH, Polgar T, Harte M, O'neill LAJ, Qwamstrom EE, Dower SK. Human tribbles, a protein family controlling mitogen-activated protein kinase cascades. *J. Biol. Chem.*, **279**, 42703–42708 (2004).
6) Örd D, Ord T. Mouse NIPK interacts with ATF4 and affects its transcriptional activity. *Exp. Cell Res.*, **286**, 308–320 (2003).
7) Ohoka N, Yoshii S, Hattori T, Onozaki K, Hayashi H. TRB3, a novel ER stress-inducible gene, is induced *via* ATF4-CHOP pathway and is involved in cell death. *EMBO J.*, **24**, 1243–1255 (2005).
8) Bezy O, Vernochet C, Gesta S, Farmer SR, Kahn CR. TRB3 blocks adipocyte differentiation through the inhibition of C/EBPbeta transcriptional activity. *Mol. Cell. Biol.*, **27**, 6818–6831 (2007).
9) Takahashi Y, Ohoka N, Hayashi H, Sato R. TRB3 suppresses adipocyte differentiation by negatively regulating PPARgamma transcriptional acltivity. *J. Lipid Res.*, **49**, 880–892 (2008).
10) Qi L, Heredia JE, Altarejos JY, Screaton R, Goebel N, Niessen S, Macleod IX, Liew CW, Kulkami RN, Bain J, Newgard C, Nelson

M, Evans RM, Yates J, Montminy M. TRB3 links the E3 ubiquitin ligase COP1 to lipid metabolism. *Science*, **312**, 1763–1766 (2006).
11) Jin G, Yamazaki Y, Takuwa M, Takahara T, Kaneko K, Kuwata T, Miyata S, Nakamura T. Trib1 and Evi1 cooperate with Hoxa and Meis1 in myeloid leukemogenesis. *Blood*, **109**, 3998–4005 (2007).
12) Dedhia PH, Keeshan K, Uljon S, Xu L, Vega ME, Shestova O, Zaks-Zilberman M, Romany C, Blacklow SC, Pear WS. Differential ability of Tribbles family members to promote degradation of C/EBPalpha and induce acute myelogenous leukemia. *Blood*, **116**, 1321–1328 (2010).
13) Xu J, Lv S, Qin Y, Shu F, Xu Y, Chen J, Xu BE, Sun X, Wu J. TRB3 interacts with CtIP and is overexpressed in certain cancers. *Biochim. Biophys. Acta*, **1770**, 273–278 (2007).
14) Sakai Y, Fukamachi K, Futakuchi M, Hayashi H, Suzui M. Promotive effects of cell proliferation and chromosomal instability induced by tribbles-related protein 3 in mouse mammary tumor cells. *Oncol. Rep.*, **30**, 64–70 (2013).
15) Kanegae Y, Lee G, Sato Y, Tanaka M, Nakai M, Sakaki T, Sugano S, Saito I. Efficient gene activation in mammalian cells by using recombinant adenovirus expressing site-specific Cre recombinase. *Nucleic Acids Res.*, **23**, 3816–3821 (1995).
16) Tanaka H, Fukamachi K, Futakuchi M, Alexander DB, Long N, Tamamushi S, Minami K, Seino S, Ohara H, Joh T, Tsuda H. Mature acinar cells are refractory to carcinoma development by targeted activation of Ras oncogene in adult rats. *Cancer Sci.*, **101**, 341–346 (2010).
17) Niwa H, Yamamura K, Miyazaki J. Efficient selection for high-expression transfectants with a novel eukaryotic vector. *Gene*, **108**, 193–199 (1991).
18) Suzui M, Inamine M, Kaneshiro T, Morioka T, Yoshimi N, Suzuki R, Kohno H, Tanaka T. Indole-3-carbinol inhibits the growth of human colon carcinoma cells but enhances the tumor multiplicity and volume of azoxymethane-induced rat colon carcinogenesis. *Int. J. Oncol.*, **27**, 1391–1399 (2005).
19) Suzui M, Masuda M, Lim JT, Albanese C, Pestell RG, Weinstein IB. Growth inhibition of human hepatoma cells by acyclic retinoid is associated with induction of p21(CIP1) and inhibition of expression of cyclin D1. *Cancer Res.*, **62**, 3997–4006 (2002).
20) Anton M, Graham FL. Site-specific recombination mediated by an adenovirus vector expressing the Cre recombinase protein: a molecular switch for control of gene expression. *J. Virol.*, **69**, 4600–4606 (1995).
21) Wagner TE, Hoppe PC, Jollick JD, Scholl DR, Hodinka RL, Gault JB. Microinjection of a rabbit beta-globin gene into zygotes and its subsequent expression in adult mice and their offspring. *Proc. Natl. Acad. Sci. U.S.A.*, **78**, 6376–6380 (1981).
22) Hogan B, Beddington R, Costantini F, Lacy E. *Manipulating the mouse embryo: a laboratory manual.* 2nd ed. (Hogan BL ed.) CSHL Press, New York, p. 220 (1994).
23) Kudoh H, Ikeda H, Kakitani M, Ueda A, Hayasaka M, Tomizuka K, Hanaoka K. A new model mouse for Duchenne muscular dystrophy produced by 2.4 Mb deletion of dystrophin gene using Cre-loxP recombination system. *Biochem. Biophys. Res. Commun.*, **328**, 507–516 (2005).
24) Law LK, Davidson BL. What does it take to bind CAR? *Mol. Ther.*, **12**, 599–609 (2005).
25) Huard J, Lochmüller H, Acsadi G, Jani A, Massie B, Karpati G. The route of administration is a major determinant of the transduction efficiency of rat tissues by adenoviral recombinants. *Gene Ther.*, **2**, 107–115 (1995).
26) Wood M, Perrotte P, Onishi E, Harper ME, Dinney C, Pagliaro L, Wilson DR. Biodistribution of an adenoviral vector carrying the luciferase reporter gene following intravesical or intravenous administration to a mouse. *Cancer Gene Ther.*, **6**, 367–372 (1999).
27) Boon ME, Kurver PJ, Baak JP, Thompson HT. The application of morphometry in gastric cytological diagnosis. *Virchows Arch. A Pathol. Anat. Histol.*, **393**, 159–164 (1981).
28) Boysen M, Reith A. Discrimination of various epithelia by simple morphometric evaluation of the basal cell layer. A light microscopic analysis of pseudostratified, metaplastic and dysplastic nasal epithelium in nickel workers. *Virchows Arch. B Cell Pathol. Incl. Mol. Pathol.*, **42**, 173–184 (1983).
29) Danielsen H, Lindmo T, Reith A. A method for determining ploidy distributions in liver tissue by stereological analysis of nuclear size calibrated by flow cytometric DNA analysis. *Cytometry*, **7**, 475–480 (1986).
30) Anthony PP, Vogel CL, Barker LF. Liver cell dysplasia: a premalignant condition. *J. Clin. Pathol.*, **26**, 217–223 (1973).
31) Clawson GA, Moody DE, James J, Smuckler EA. Nuclear envelope alterations accompanying thioacetamide-related enlargement of the nucleus. *Cancer Res.*, **41**, 519–526 (1981).
32) Enzmann H, Kühlem C, Löser E, Bannasch P. Dose dependence of diethylnitrosamine-induced nuclear enlargement in embryonal turkey liver. *Carcinogenesis*, **16**, 1351–1355 (1995).
33) Wiemann C, Enzmann H, Löser E, Schlüter G. Nonlinearity of nuclear enlargement in hepatocytes induced by the carcinogen *N'*-nitrosomorpholine *in vivo*. *Cancer Detect. Prev.*, **23**, 485–495 (1999).
34) Koo SH, Satoh H, Herzig S, Lee CH, Hedrick S, Kulkarni R, Evans RM, Olefsky J, Montminy M. PGC-1 promotes insulin resistance in liver through PPARalpha-dependent induction of TRB-3. *Nat. Med.*, **10**, 530–534 (2004).

RESEARCH ARTICLE

Comparative Study of Toxic Effects of Anatase and Rutile Type Nanosized Titanium Dioxide Particles *in vivo* and *in vitro*

Takamasa Numano[1,3], Jiegou Xu[2], Mitsuru Futakuchi[1], Katsumi Fukamachi[1], David B Alexander[2], Fumio Furukawa[3], Jun Kanno[4], Akihiko Hirose[4], Hiroyuki Tsuda[2], Masumi Suzui[1]*

Abstract

Two types of nanosized titanium dioxide, anatase ($anTiO_2$) and rutile ($rnTiO_2$), are widely used in industry, commercial products and biosystems. TiO_2 has been evaluated as a Group 2B carcinogen. Previous reports indicated that $anTiO_2$ is less toxic than $rnTiO_2$, however, under ultraviolet irradiation $anTiO_2$ is more toxic than $rnTiO_2$ *in vitro* because of differences in their crystal structures. In the present study, we compared the *in vivo* and *in vitro* toxic effects induced by $anTiO_2$ and $rnTiO_2$. Female SD rats were treated with 500 μg/ml of $anTiO_2$ or $rnTiO_2$ suspensions by intra-pulmonary spraying 8 times over a two week period. In the lung, treatment with $anTiO_2$ or $rnTiO_2$ increased alveolar macrophage numbers and levels of 8-hydroxydeoxyguanosine (8-OHdG); these increases tended to be lower in the $anTiO_2$ treated group compared to the $rnTiO_2$ treated group. Expression of MIP1α mRNA and protein in lung tissues treated with $anTiO_2$ and $rnTiO_2$ was also significantly up-regulated, with MIP1α mRNA and protein expression significantly lower in the $anTiO_2$ group than in the $rnTiO_2$ group. In cell culture of primary alveolar macrophages (PAM) treated with $anTiO_2$ and $rnTiO_2$, expression of MIP1α mRNA in the PAM and protein in the culture media was significantly higher than in control cultures. Similarly to the *in vivo* results, MIP1α mRNA and protein expression was significantly lower in the $anTiO_2$ treated cultures compared to the $rnTiO_2$ treated cultures. Furthermore, conditioned cell culture media from PAM cultures treated with $anTiO_2$ had less effect on A549 cell proliferation compared to conditioned media from cultures treated with $rnTiO_2$. However, no significant difference was found in the toxicological effects on cell viability of ultra violet irradiated $anTiO_2$ and $rnTiO_2$. In conclusion, our results indicate that $anTiO_2$ is less potent in induction of alveolar macrophage infiltration, 8-OHdG and MIP1α expression in the lung, and growth stimulation of A549 cells *in vitro* than $rnTiO_2$.

Keywords: Nanosized titanium dioxide - anatase - rutile - lung toxicity - MIP1α

Asian Pac J Cancer Prev, **15 (2)**, 929-935

Introduction

There are three mineral forms of natural titanium dioxide particles: rutile, anatase and brookite. Engineered anatase and rutile nanosized titanium dioxide particles ($anTiO_2$ and $rnTiO_2$) are being manufactured in large quantities worldwide and applied in many fields including material industry, electronic industry, commercial products and biosystems. Due to differences in crystal structure, $anTiO_2$ has better photocatalytic activity than $rnTiO_2$ (Kakinoki et al., 2004). Accordingly, $anTiO_2$ is mainly used in paints, such as surface painting of the walls and windows of buildings and vehicles, and photocatalytic systems, while $rnTiO_2$ is preferentially used in cosmetics, sunscreen and food additives.

Large quantity production and widespread application of $nTiO_2$ have given rise to concern about its health and environmental effects. Anatase and rutile type titanium dioxide particles, nanosized and larger, are evaluated as Group 2B carcinogens (possibly carcinogenic to humans) by WHO/International Agency for Research on Cancer (IARC, 2010), based on 2-year animal aerosol inhalation studies (Mohr et al., 2006). Pulmonary exposure to $rnTiO_2$ promotes DHPN-induced lung carcinogenesis in rats, and the promotion effect is possibly associated with $rnTiO_2$ burdened alveolar macrophage derived macrophage inflammatory protein 1 alpha (MIP1α), which acts as a growth factor to stimulate the proliferation of human lung adenocarcinoma cells (A549) *in vitro* (Xu et al., 2010). Dermal application of $anTiO_2$ has been shown to cause significant increases in the level of superoxide dismutase and malondialdehyde in hairless mice (Wu et al., 2009).

Size and photoactivation affect the *in vitro* toxicity of $anTiO_2$ and $rnTiO_2$. $anTiO_2$ (10 and 20 nm) induces

[1]*Department of Molecular Toxicology, Nagoya City University Graduate School of Medical Sciences and Medical School,* [2]*Laboratory of Nanotoxicology Project, Nagoya City University, Nagoya,* [3]*DIMS Institute of Medical Science, Aichi,* [4]*National Institute of Health Sciences, Tokyo, Japan* **For correspondence: suzui@med.nagoya-cu.ac.jp*